A 2-D Range Ambiguity Suppression Method Based on Blind Source Separation for Multichannel SAR Systems

Ershad Junus Amin, Gerhard Krieger, *Fellow, IEEE*, Marwan Younis, *Fellow, IEEE*, Federica Bordoni, André Barros Cardoso da Silva, and Alberto Moreira, *Fellow, IEEE*

***Abstract*— Advanced multichannel spaceborne synthetic aperture radar (SAR) systems with multiple elevation beams allow for obtaining high-resolution and wide-swath SAR images. However, the degradation of the SAR image quality due to range ambiguities is still an issue. In this article, the range-ambiguity problem is analytically modeled and solved by employing a range-time and Doppler-frequency dependent mixing matrix, which describes the linear superposition of multiple mutually range-ambiguous radar echoes. The overall framework can be regarded as a generalization of the cocktail party problem where each listener has to separate one speech signal out of a linear superposition of multiple voices. For the first time, the 2-D dependence of the antenna radiation pattern in the elevation and azimuth directions is considered by accounting for both the real-time beamsteering in elevation and the systematic variations of the mixing coefficients with the Doppler frequency. A novel solution, based on higher order blind source separation, is presented. The performance of the proposed method is numerically analyzed, with reference to an array-fed reflector antenna SAR system, by simulating a realistic acquisition scenario. To this aim, real-SAR data and the actual antenna patterns of the Tandem-L mission proposal are considered.**

***Index Terms*— Digital beamforming (DBF), echo separation, high-resolution wide-swath, independent component analysis, reflector antenna, spaceborne synthetic aperture radar (SAR).**

I. Introduction

SYNTHETIC aperture radar (SAR) is one of the most relevant techniques for Earth observation. Conventional SAR images, however, still suffer from a tradeoff between the extension of the imaged swath and the spatial resolution [1]. In order to overcome this limitation, novel system architectures and operational modes, exploiting multiple digital receive channels, have been intensely studied and developed in the last decades. Important examples of these kinds of systems are the U.S.–Indian NISAR, scheduled for launch in 2023, and the German mission proposal Tandem-L (TDL) [2], [3]. Here, in order to overcome the tradeoff between swath extension and azimuth resolution, a wide swath is illuminated by a broad transmit beam, at high pulse repetition frequency (PRF). On receive, multiple elevation beams simultaneously collect the useful signals returned from the swath. Each receive beam operates according to the scan-on-receive (SCORE) digital beamforming (DBF) technique [4], [5]. Both in the case of NISAR and TDL, the SAR architecture is based on an array-fed reflector antenna. In fact, compared with a planar antenna, this architecture has a limited hardware complexity and allows to obtain antenna radiation patterns with a higher gain and lower sidelobes [6].

The main challenge of such a multibeam operational mode is the separation of the useful signals from each other. In fact, the signal that is useful for one receive beam represents a range ambiguity for another beam. Accordingly, the range ambiguities cannot be attenuated by the transmit pattern, as in a conventional case where only a single-Rx beam is used. This issue can be hardly tackled by state-of-the-art techniques for range ambiguity suppression, such as azimuth phase coding (APC) [7], [8], waveform encoding [9], staggered SAR [10], [11], especially without a significant impact on the SAR instrument complexity.

In principle, in order to suppress the range ambiguities, DBF techniques, such as minimum variance distortionless response (MVDR), could be used to realize receive patterns with very low sidelobe levels [6], [12], or linearly constrained minimum variance (LCMV) which place nulls in the expected directions of arrival of the ambiguous signals [13], [14]. However, in practice, the knowledge of the pattern may be insufficient to achieve a satisfactory ambiguity suppression. In fact, due to the large size of the reflector, it is impossible to accurately calibrate the pattern on the ground, before the launch. Moreover, the actual pattern may considerably differ from the expected one, due to deviations of the reflector surface from its nominal shape after the reflector deployment or deformations associated with temperature variations, satellite mispointing, as well as phase offsets among the individual receive channels. Also, the topography may impact the range ambiguity suppression, and a topographic error of 1.5 km may raise the range ambiguity to an unacceptable level of -17 dB [15]. The problem related to the poor knowledge of the pattern is not solved properly even by in-orbit pattern calibration approaches. In fact, most of these methods require the availability of homogeneous backscattering surfaces with a flat topography [16], [17], [18].

In this article, the range ambiguity suppression problem is recast in the framework of the cocktail party phenomenon [19]. To suppress the range ambiguities, a novel

Manuscript received 6 April 2023; revised 23 August 2023 and 2 November 2023; accepted 16 December 2023. Date of publication 17 January 2024; date of current version 31 January 2024. *(Corresponding author: Ershad Junus Amin.)*

The authors are with the Microwaves and Radar Institute, German Aerospace Center, 82234 Weßling, Germany (e-mail: ershad.amin@dlr.de).

Digital Object Identifier 10.1109/TGRS.2024.3355149

data-based approach is proposed, using a higher order blind source separation (BSS) technique on the downlinked data. The remarkable aspect of this method is that it does not require any prior knowledge of the actual antenna pattern. While the degradation of the range ambiguity suppression performance for most of the techniques mentioned earlier is directly related to the increasing deviation of the actual pattern from the nominal pattern, in contrast, the proposed method maintains its robustness even in this case, as it estimates the necessary information on the actual pattern, i.e., the mixing coefficients, directly from the acquired SAR data to suppress range ambiguities. This represents a significant advantage of the method over the majority of range ambiguity suppression techniques. Additionally, it does not affect the SAR instrument complexity.

The idea behind the proposed method was originally proposed in [15] as one opportunity to obtain the calibration coefficients for the cross elevation beam range ambiguity suppression technique CEBRAS; first results, presented already in short conference papers [20], [21], are here extended and analyzed in detail. A BSS-based method, to retrieve the useful SAR signals in a multibeam SAR system, was recently proposed also in [22] and [23]. Compared with these last publications, the uniqueness and novelty of the present approach rely on the detailed data model and the realistic analysis. Specifically, the 2-D dependence of the antenna radiation patterns and of the SAR signals versus range time and Doppler frequency is considered and integrated into the implementation of the BSS technique. Furthermore, attention is given to noise in the data model. The performance of the proposed method is numerically analyzed in realistic scenarios, simulated by means of real SAR data and the actual antenna patterns of TDL [6], [12].

This article is organized as follows. In Section II-A, the general concept of the cocktail party problem is reviewed, followed by a novel derivation of the extended cocktail party problem for multichannel SAR in Section II-B. The proposed 2-D range ambiguity suppression method based on higher order BSS is presented in Section III. Section IV reports the numerical analysis. The importance of the method in the research field is discussed in Section V. Section VI concludes this article.

II. Problem Formulation

A. Cocktail Party Problem

Let us consider several people talking simultaneously at a cocktail party. Each person hears different voices, which are mixed together. This phenomenon can be modeled as [24]

$$\mathbf{x}(t) = \mathbf{A} \cdot \mathbf{s}(t)$$
$$\begin{bmatrix} x_1(t) \\ \vdots \\ x_M(t) \end{bmatrix} = \begin{bmatrix} a_{1,1} & \cdots & a_{1,N} \\ \vdots & \ddots & \vdots \\ a_{M,1} & \cdots & a_{M,N} \end{bmatrix} \cdot \begin{bmatrix} s_1(t) \\ \vdots \\ s_N(t) \end{bmatrix} \tag{1}$$

where M is the number of listeners; N the number of people talking; $\mathbf{A}$ is the mixing matrix, with elements given by the mixing coefficients; $\mathbf{x}$ the vector of the M heard mixed voices; and $\mathbf{s}$ the vector of the N emitted speech signals. The so-called "cocktail party problem" denotes then the task of extracting the useful source signals, $\mathbf{s}$, from the received ones, $\mathbf{x}$, without knowing $\mathbf{A}$ (see Fig. 1).

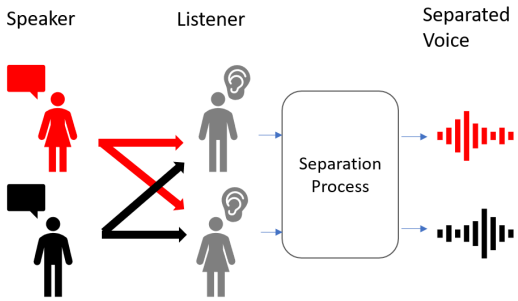

Fig. 1. Illustration of the cocktail party problem.

It is worth noting that when $M = N$, each emitted voice represents the useful signal for one listener and the disturbance of variable strength for the others. This property of the source signals is denoted as reciprocity. As shown in the next sections, it is of key importance in the multichannel SAR context.

B. Cocktail Party Problem in Multichannel SAR

Without loss of generality, let us consider a multichannel SAR system, based on an array-fed reflector, like TDL [2]. As shown in Fig. 2, multiple subswaths are imaged simultaneously, by means of a wide transmit (Tx) beam that illuminates the whole swath, and multiple narrow receive (Rx) beams (each one dedicated to a subswath) that follow the echo on the ground in the elevation direction, according to the SCORE technique [5], [25].

Since the PRF is high w.r.t. the overall swath extension, range ambiguous echoes are received from the imaged swath. In particular, the received signal can be expressed as

$$x_i(\tau, f_t) = s_i(\tau, f_t) + \sum_m s_{i,\mathrm{RA}}(\tau, f_t, m) \tag{2}$$

where x_i denotes the signal received from the ith beam; s_i and $s_{i,\mathrm{RA}}$ are the corresponding useful signal and range ambiguous signals, respectively, which are simultaneously received; τ is the range time; f_t is the Doppler frequency; and m is the order of ambiguity.

The slant range of the range ambiguous target is given by

$$R_{\mathrm{RA}} = R_0 + D_r(m) \tag{3}$$

where R_0 is the slant range of the useful target, and D_r is the distance of ambiguity, i.e., the slant range displacement between useful signal and range ambiguous signal is given by

$$D_r(m) = \frac{m \cdot c \cdot \mathrm{PRI}}{2} \tag{4}$$

where PRI is the pulse repetition interval; and c is the speed of light.

It is worth mentioning that strong range ambiguities arise within the imaged swath due to the Tx pattern that illuminates them. Ambiguities that arise outside the imaged swath are much lower and referred to as weak ambiguities.[1]

[1]The nadir echo is considered a weak ambiguity, as it is assumed to be sufficiently suppressed, not only by the Tx and Rx beams but eventually also by specific techniques, such as [26] and [27].

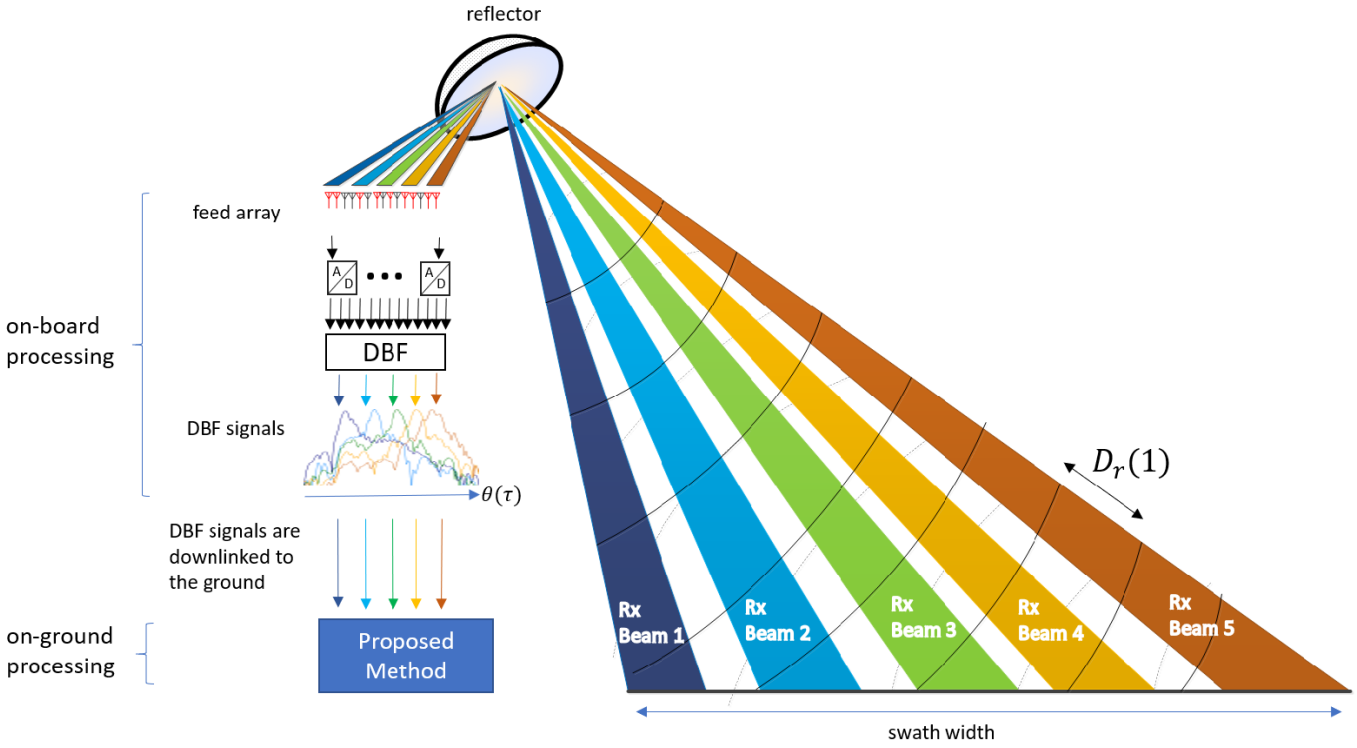

Fig. 2. Multichannel SAR system, based on an array-fed reflector, imaging five subswaths simultaneously by means of five SCORE Rx beams. The five SCORE-received signals are downloaded to the ground, where the proposed method is applied.

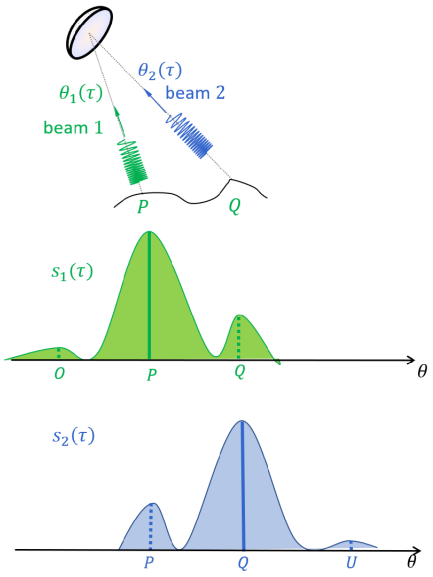

Fig. 3. Zero-Doppler geometry. Two subswaths are imaged simultaneously by two beams. In beam 1, P returns the useful signal, Q the strong ambiguity; in beam 2, Q returns the useful signal, and P the strong ambiguity.

As a consequence, as first mentioned in [15], a reciprocity property exists between the useful signals and the ambiguity signals. Accordingly, the ambiguity of a useful signal is always represented by a scaled version of another useful signal, where the scaling factor is given by a complex number.

To further explain the reciprocity, let us consider the scenario in Fig. 3, characterized by two Rx beams and four target points (O, P, Q, and U), separated by the distance of ambiguity. Based on (2), the two Rx signals can be expressed as

$$\begin{aligned} x_1(\tau, f_t) &= s_1(\tau, f_t) + \sum_m s_{1,\mathrm{RA}}(\tau, f_t, m) \\ &= \sigma_P \cdot w_1(\tau, f_t, P) \cdot \mathrm{rect}\left(\tau - \frac{2R_P(f_t)}{c}\right) \\ &\quad \cdot \exp\left(-j\frac{4\pi}{\lambda}R_P(f_t)\right) \cdot \exp\left(j\pi k_r\left[\tau - \frac{2R_P(f_t)}{c}\right]^2\right) \\ &\quad + \sigma_Q \cdot w_1(\tau, f_t, Q) \cdot \mathrm{rect}\left(\tau - \frac{2R_Q(f_t)}{c}\right) \\ &\quad \cdot \exp\left(-j\frac{4\pi}{\lambda}R_Q(f_t)\right) \cdot \exp\left(j\pi k_r\left[\tau - \frac{2R_Q(f_t)}{c}\right]^2\right) \\ &\quad + \sigma_O \cdot w_1(\tau, f_t, O) \cdot \mathrm{rect}\left(\tau - \frac{2R_O(f_t)}{c}\right) \\ &\quad \cdot \exp\left(-j\frac{4\pi}{\lambda}R_O(f_t)\right) \cdot \exp\left(j\pi k_r\left[\tau - \frac{2R_O(f_t)}{c}\right]^2\right) \end{aligned} \tag{5}$$

$$\begin{aligned} x_2(\tau, f_t) &= s_2(\tau, f_t) + \sum_m s_{2,\mathrm{RA}}(\tau, f_t, m) \\ &= \sigma_Q \cdot w_2(\tau, f_t, Q) \cdot \mathrm{rect}\left(\tau - \frac{2R_Q(f_t)}{c}\right) \\ &\quad \cdot \exp\left(-j\frac{4\pi}{\lambda}R_Q(f_t)\right) \cdot \exp\left(j\pi k_r\left[\tau - \frac{2R_Q(f_t)}{c}\right]^2\right) \end{aligned}$$

$$+\sigma_P \cdot w_2(\tau, f_t, P) \cdot \text{rect}\left(\tau - \frac{2R_P(f_t)}{c}\right) \cdot \exp\left(-j\frac{4\pi}{\lambda}R_P(f_t)\right) \cdot \exp\left(j\pi k_r\left[\tau - \frac{2R_P(f_t)}{c}\right]^2\right) + \sigma_U \cdot w_2(\tau, f_t, U) \cdot \text{rect}\left(\tau - \frac{2R_U(f_t)}{c}\right) \cdot \exp\left(-j\frac{4\pi}{\lambda}R_U(f_t)\right) \cdot \exp\left(j\pi k_r\left[\tau - \frac{2R_U(f_t)}{c}\right]^2\right) \tag{6}$$

where $w(\tau, f_t, Y)$ denotes the two-way antenna pattern, weighting the signal received from the point Y ($Y = O, P, Q, U$);[2] σ_Y is the complex amplitude of the echo received from Y; R_Y is the distance between the receiver and Y; and k_r and λ are the transmitted chirp rate and the radar wavelength, respectively. It is noted that in the raw data, the Doppler frequency band is determined by the illumination time. However, the azimuth envelope is omitted in the equation for a simpler representation.

It is important to note that the derivation in (5) and (6) can be generalized to distributed targets. Specifically, while in the point target case $Y = O, P, Q$, and U represent individual point targets, in the distributed target case $Y = O, P, Q$, and U represent range bins. In the distributed target case, the received signal at a range bin consists of multiple scattering points.

The strong ambiguity signal, s_{SA}, comes from Q in (5), or P in (6); the weak ambiguity, s_{WA}, comes from O and U. It is then useful to compare the strong ambiguity, $s_{1,\text{SA}}$, in (5) to the useful signal, s_2 in (6)

$$s_{1,\text{SA}}(\tau, f_t) = \sigma_Q \cdot w_1(\tau, f_t, Q) \cdot \text{rect}\left(\tau - \frac{2R_Q(f_t)}{c}\right) \cdot \exp\left(-j\frac{4\pi}{\lambda}R_Q(f_t)\right) \cdot \exp\left(j\pi k_r\left[\tau - \frac{2R_Q(f_t)}{c}\right]^2\right) \tag{7}$$

$$s_2(\tau, f_t) = \sigma_Q \cdot w_2(\tau, f_t, Q) \cdot \text{rect}\left(\tau - \frac{2R_Q(f_t)}{c}\right) \cdot \exp\left(-j\frac{4\pi}{\lambda}R_Q(f_t)\right) \cdot \exp\left(j\pi k_r\left[\tau - \frac{2R_Q(f_t)}{c}\right]^2\right). \tag{8}$$

From (7) and (8), it can be seen that the two signals differ only by a complex constant, given by the relative antenna pattern level of w_1 and w_2 at the location Q. This shows that the range ambiguity level is solely determined by the ratio between the sidelobe and mainlobe of the antenna patterns

$$a_{12}(\tau, f_t) = \frac{s_{1,\text{SA}}(\tau, f_t)}{s_2(\tau, f_t)} = \frac{w_1(\tau, f_t, Q)}{w_2(\tau, f_t, Q)} \tag{9}$$

[2]In the following, for simplicity, it is assumed that the signal, received from a point target, is weighted by the pattern value at the target location, i.e., the SCORE beam movement during the pulse duration, particularly for long pulse, is neglected [28].

$$a_{21}(\tau, f_t) = \frac{s_{2,\text{SA}}(\tau, f_t)}{s_1(\tau, f_t)} = \frac{w_2(\tau, f_t, P)}{w_1(\tau, f_t, P)} \tag{10}$$

where a_{12} is the mixing coefficient between the strong ambiguity signal $s_{1,\text{SA}}$ and the useful signal s_2, and a_{21} is the mixing coefficient between strong ambiguity signal $s_{2,\text{SA}}$ to useful signal s_1.

Accordingly, (5) and (6) can be rewritten as follows:

$$x_1(\tau, f_t) = s_1(\tau, f_t) + a_{12}(\tau, f_t) \cdot s_2(\tau, f_t) + s_{1,WA}(\tau, f_t) \tag{11}$$

$$x_2(\tau, f_t) = s_2(\tau, f_t) + a_{21}(\tau, f_t) \cdot s_1(\tau, f_t) + s_{2,WA}(\tau, f_t). \tag{12}$$

Based on (5)–(12), the general case of N-elevation Rx beams which map N-subswaths and accounting for white Gaussian noise $\mathbf{n}$, can be written as

$$\mathbf{x}(\tau, f_t) = \mathbf{A}(\tau, f_t) \cdot \mathbf{s}(\tau, f_t) + \mathbf{s}_{\text{WA}}(\tau, f_t) + \mathbf{n}$$

$$\begin{bmatrix} x_1(\tau, f_t) \\ \vdots \\ x_N(\tau, f_t) \end{bmatrix} = \begin{bmatrix} 1 & \cdots & a_{1,N}(\tau, f_t) \\ \vdots & \ddots & \vdots \\ a_{N,1}(\tau, f_t) & \cdots & 1 \end{bmatrix} \cdot \begin{bmatrix} s_1(\tau, f_t) \\ \vdots \\ s_N(\tau, f_t) \end{bmatrix} + \begin{bmatrix} s_{1,WA}(\tau, f_t) \\ \vdots \\ s_{N,WA}(\tau, f_t) \end{bmatrix} + \begin{bmatrix} n_1 \\ \vdots \\ n_N \end{bmatrix}. \tag{13}$$

It is important to note that the received SAR signals, $\mathbf{x}$, the useful signals, $\mathbf{s}$, and the mixing matrix, $\mathbf{A}$, depend on range time, τ, and Doppler frequency, f_t. In particular, $\mathbf{A}$ represents the relative value of the sidelobe to the mainlobe of the two-way pattern, as written in (9) and (10). Accordingly, the diagonal elements, which correspond to the useful signal, are unitary; while the off-diagonal elements, which correspond to the range ambiguities, are complex coefficients, with amplitude lower than 1. In particular, the off-diagonal elements of the SAR mixing matrix are in general much lower than 1 (i.e., the SAR mixing matrix is considerably "low"), since the Rx antenna patterns are typically designed to suppress the undesired strong ambiguities [6]. Moreover, the off-diagonal values of $\mathbf{A}$ show a strong variation versus τ and a moderated variation versus f_t since the useful and ambiguous signal have a large angular separation in the range direction but are both located around zero-Doppler.

With reference to (13), the problem to be solved in the multichannel SAR context is to suppress the range ambiguities by extracting the N useful signals, $\mathbf{s}$, from the N received mixed signals, $\mathbf{x}$. The similarity with the cocktail party problem, described in Section II-A, is evident. In particular, also in the SAR case, the reciprocity property applies, and the mixing matrix is unknown. The main differences regard: 1) the presence in the SAR signal of the weak ambiguous signals, s_{WA}, and the white-Gaussian noise n and 2) the dependence of the SAR mixing matrix and signal on the range time and Doppler frequency. Based on this dependence, the range ambiguity suppression problem is denoted as 2-D.

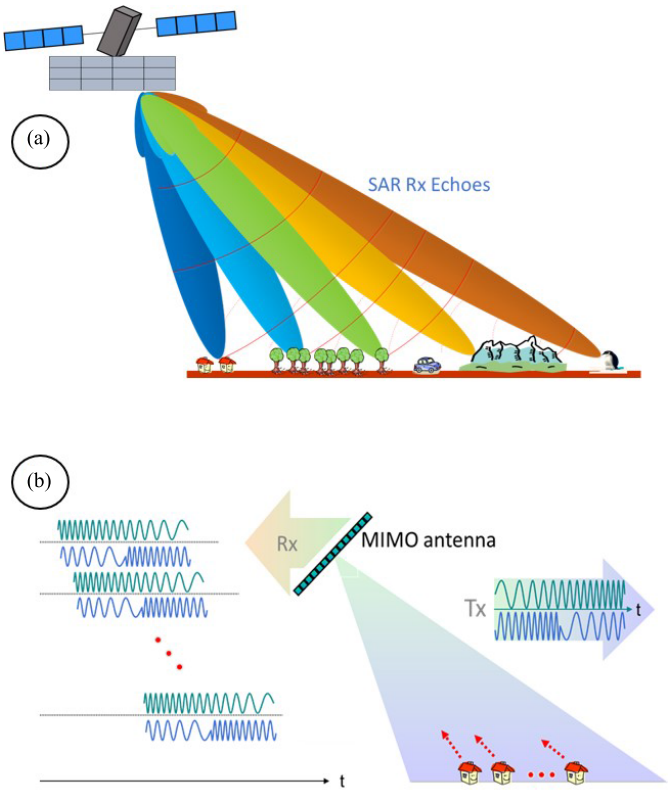

Fig. 4. Example of SAR systems where the cocktail party problem can be applied. (a) Multichannel SAR system, based on a planar array antenna with multiple elevation Rx beams. (b) Waveform-encoding MIMO-SAR [29], [30].

It is worth mentioning that the noise does not provide any information about the mixing matrix. In fact, as shown in (13), it is introduced by each receive channel on the already combined useful signals, $\mathbf{s}$. Accordingly, an increasing noise level may make the extraction of the N useful signals more challenging, as explained more in detail in Section III.

Finally, it is worth noting that the reported derivation is not limited to the case of monostatic array-fed reflector antenna SAR systems. In fact, as illustrated in Fig. 4, it can be easily be extended to planar array antenna systems or MIMO-SAR systems [29], [30].

III. Proposed Method

A. Higher Order Blind Source Separation

The method proposed in this article to tackle the range ambiguity suppression problem in (13) is based on the BSS technique [31]. In the classical cocktail party problem, the BSS estimates the useful signals, i.e., the emitted voices, as

$$\hat{\mathbf{s}} = \mathbf{B}\mathbf{x} \tag{14}$$

where $\mathbf{B}$ is the separation matrix. This solution is in general not unique. In fact, it is affected by scaling and permutation uncertainties, since both the useful source signals, $\mathbf{s}$, and the mixing matrix, $\mathbf{A}$, are unknown [31].

The BSS methods can be separated into two categories: second-order methods, which rely on the assumption, that the source signals are mutually uncorrelated (in the sense of classical second-order correlations) [32], [33]; the higher order BSS methods, which rely on the mutual independence among all source signals [34], [35]. It is worth mentioning that, in general, the SAR mixing matrix poses a challenge to the BSS. In fact, the BSS method relies on the statistical properties of the source signals (correlation for the second-order, independence for the higher order), and the sensitivity of the method depends on the statistical differences between the useful signal and the received signal [33], [34]. Accordingly, when the mixing matrix is considerably low (see Section II), the statistical difference between the useful and the received signals becomes relatively small, reducing the sensitivity of the BSS method. Moreover, in the SAR context, the noise produces a model mismatch and is expected to degrade the BSS performance, since it does not provide any information on the mixing matrix, as shown by (13). In particular, the higher order BSS approach is expected to offer a greater robustness to the noise compared to the second-order [36], [37], [38]. In this article, as higher order BSS, the joint approximation diagonalization of eigenvalue (JADE) is considered [35], [39].

The idea behind the higher order BSS methods comes from the central limit theorem [40], which states that the sum of an infinitely large number of independent random variables will result in a Gaussian random variable. Accordingly, in the cocktail party problem, even in the presence of a limited number of source signals, the received signals are expected to be more Gaussian than the useful source signals. This property is exploited by the higher order BSS methods to estimate the useful signals [31]. In particular, the higher order BSS algorithms consist of two steps: first, the principal component analysis (PCA), which removes the second-order correlation of the input data; second, the independent component analysis (ICA), which obtains independent signals by exploiting their higher order statistics.

In the multichannel SAR context, the BSS separation matrix assumes the form

$$\mathbf{B} \approx \mathbf{A}^{-1} \tag{15}$$

where the approximation derives from the model mismatch between (13) and (1), due to the presence of weak ambiguities and the additive noise. As regards the uniqueness of the solution, the scaling and permutation uncertainties are not an issue. In fact, they can be solved by exploiting the information on the unitary diagonal elements of the SAR mixing matrix (see Section II-B).

It is worth mentioning that a precondition for a successful application of the higher order BSS methods is the non-Gaussianity of the useful signals [31], [41]. In the context of SAR, the various types of terrain and terrain cover exhibit distinct Gaussianity characteristics [1]. These differences in backscatter statistics can significantly affect the effectiveness of the method. Additionally, as discussed in more detail in Section III-B, the selection of the kind of SAR data should be carefully considered in order to properly apply the BSS in the SAR context. Moreover, the performance of BSS is also affected by the relative intensity level of the ambiguous and useful components. In particular, for very weak ambiguities, the Gaussianity of the source and received signals may be similar, and consequently, the successful application of the BSS method is challenging. Accordingly, the SAR mixing

matrix, and specifically the low amplitude of the off-diagonal elements, is expected to strongly affect the achievable BSS performance. The presence of additive white Gaussian noise may also degrade the performance. Another challenge for the application of the BSS in the SAR context is the dependence of both the mixing matrix and the useful signals on the range time and Doppler frequency. In fact, the JADE method is classified as a stationary technique [42], [43], [44]. Accordingly, proper steps should be introduced to improve the BSS performance. This is discussed more in detail in Section III-C.

B. SAR Range Compressed Data

Let us consider the main three kinds of SAR data: raw data, range compressed data, and fully focused image. The selection of the input SAR data for the BSS is here driven by the Gaussianity level and the reciprocity of these signals.

The SAR raw data are considered not suitable since they are characterized by the highest Gaussianity. In fact, each sample collects the backscattering from the widest area, given by the instantaneous radar field of view [45].

The focused SAR image, at least for a heterogeneous scene, can be assumed to have non-Gaussian statistics [46], [47]. Nevertheless, fully focused SAR data do not satisfy the reciprocity between the useful and ambiguous signals as written in (13). The problem arises during the azimuth compression step, due to the different azimuth FM rates between the useful signal and the range ambiguity signal. In particular, the azimuth FM rate can be expressed as follows [48]:

$$K_a(R) = \frac{2V_r^2}{\lambda R} \tag{16}$$

where V_r denotes the effective radar velocity; and R is the minimum slant range of the imaged point-target/resolution cell, as in (3).

Recalling the problem discussed in Section II, the range ambiguity signal and the useful signal in (7) and (8), after azimuth compression, can be written as follows:

$$s''_{1,\mathrm{SA}}(\tau, f_t) = \sigma_Q \cdot w''_1(\tau, f_t, Q) \cdot \delta\left(\tau - \frac{2R_Q}{c}\right) \cdot \exp\left(-j\frac{4\pi}{\lambda}R_Q\right) \cdot \exp\left(-j\frac{\pi\lambda D_r f_t^2}{2V_r^2}\right) \tag{17}$$

$$s''_2(\tau, f_t) = \sigma_Q \cdot w''_2(\tau, f_t, Q) \cdot \delta\left(\tau - \frac{2R_Q}{c}\right) \cdot \exp\left(-j\frac{4\pi}{\lambda}R_Q\right) \tag{18}$$

where D_r is the distance of the ambiguity, here computed for $m = 1$; $\delta(\tau)$ is the range impulse response after range focusing; and the symbol $''$ is used to denote the focused image case. According to (17) and (18), the strong ambiguity signal, $s''_{1,\mathrm{SA}}$, and the useful signal, s''_2, do not differ by a complex constant, and the reciprocity is no more valid.

The reciprocity between signals, separated by the ambiguity distance, is still preserved in the range-compressed domain

$$s'_{1,\mathrm{SA}}(\tau, f_t) = \sigma_Q \cdot w'_1(\tau, f_t, Q) \cdot \delta\left(\tau - \frac{2R_Q(f_t)}{c}\right) \cdot \exp\left(-j\frac{4\pi R_Q}{\lambda}\right) \cdot \exp\left(j\pi\frac{f_t^2}{K_a(R_Q)}\right) \tag{19}$$

$$s'_2(\tau, f_t) = \sigma_Q \cdot w'_2(\tau, f_t, Q) \cdot \delta\left(\tau - \frac{2R_Q(f_t)}{c}\right) \cdot \exp\left(-j\frac{4\pi R_Q}{\lambda}\right) \cdot \exp\left(j\pi\frac{f_t^2}{K_a(R_Q)}\right) \tag{20}$$

where the symbol $'$ is used to denote the range compressed domain. In fact, (19) and (20) differ only by a complex constant

$$a'_{12}(\tau, f_t) = \frac{s'_{1,\mathrm{SA}}}{s'_2} = \frac{w'_1(\tau, f_t, Q)}{w'_2(\tau, f_t, Q)}. \tag{21}$$

With regards to the statistics, the range-compressed data have a higher deviation from Gaussianity compared with the raw data, as the range compression enhances the contrast in the range direction due to its focusing properties. Therefore, applying the BSS in the range-compressed domain appears as the best choice.

It must be remarked that no range cell migration (RCM) correction should be applied to the selected range-compressed data, in order to preserve the reciprocity. In fact, after RCM correction, the range envelope of the useful signal is already independent of Doppler frequency, while the range envelope of the range ambiguity is still a function of Doppler frequency due to the only partially corrected RCM (see Fig. 5). More in detail, it can be derived that the maximum residual RCM affecting the ambiguous signal is approximately given by

$$\Delta\mathrm{RCM} = \frac{\lambda^2 D_r(m)}{32\,\delta_{\mathrm{az}}^2} \tag{22}$$

where δ_{az} denotes the azimuth resolution. From (22), it is clear that the residual RCM may not be an issue for X-band SAR systems with a moderate azimuth resolution, but cannot be neglected in L-band systems.

The reciprocity of the selected range compressed data is illustrated in Fig. 6 for different scenarios. For instance, the reciprocity happens between s_2 and s_6 in zero Doppler, with a mixing coefficient a_{26}. In the nonzero Doppler, the reciprocity happens between s_1 and s_4, with a mixing coefficient a_{14}.[3] The fact that the value of the mixing coefficient is changing along the Doppler requires an optimization strategy, as discussed in Section III-C.

C. Performance Optimization

Two different novel strategies are included in the proposed method, in order to improve the BSS performance in the multichannel SAR context. They are denoted as stacking and azimuth subband decomposition, respectively.

The implementation of BSS alone, without additional optimization strategies, does not lead to satisfactory range ambiguity-to-signal ratio (RASR) performance, as shown later

[3]The main purpose of showing Figs. 5 and 6 is to visually assess the signal's reciprocity principle, which is of significant importance for the BSS technique. To ensure a fair assessment, a comparison is conducted using the same range-bin reference for both Figs. 5 and 6, despite the fact that the signals in Figs. 5(c) and 6(c) are different due to the presence of the RCM effect.

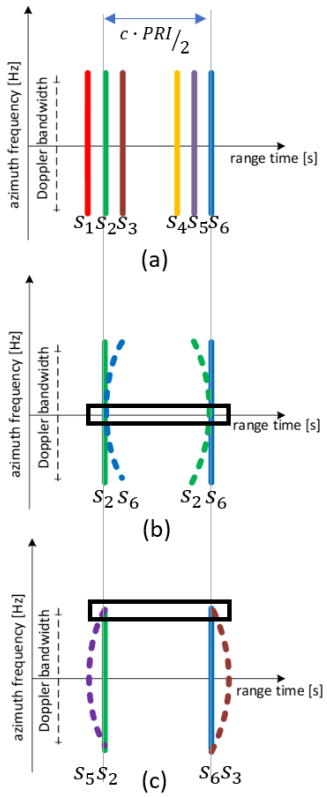

Fig. 5. Violation of signal reciprocity after RCM correction. Useful signals denoted by a solid curve, the range ambiguous signals denoted by dotted curves. Left and right signals separated by the range ambiguity distance $c \cdot \mathrm{PRI}/2$, indicated by the vertical line: (a) six useful signals s_1–s_6 after RCM correction; (b) range ambiguity in zero Doppler (area inside the black box), the received signal is composed by $s_2 + s_6$; and (c) range ambiguity in nonzero Doppler (area inside the black box), on the left the received signal is $s_5 + s_2$, while on the right, the received signal is $s_6 + s_3$.

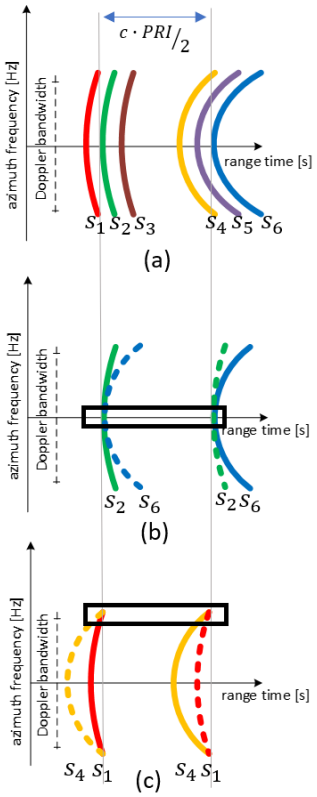

Fig. 6. Reciprocity before RCM correction. Left and right signals separated by range ambiguity distance $c \cdot \mathrm{PRI}/2$, indicated by the vertical lines. Useful signals denoted by a solid curve, range ambiguous signals denoted by dotted curves: (a) six useful signals s_1–s_6 before RCM correction; (b) range ambiguity in zero Doppler (area inside the black box), received signal composed by $s_2 + s_6$; (c) range ambiguity in nonzero Doppler (area inside the black box), received signal is composed by $s_4 + s_1$.

in numerical analysis (Section IV). This constraint arises from the biased estimation of the kurtosis when dealing with the limited amount of data [49]. It is worth highlighting that the effectiveness of BSS strongly depends on an accurate estimation of the kurtosis. Therefore, it becomes essential to employ suitable approaches, such as the stacking strategy in this case. Additionally, considering that the range ambiguity problem is formulated as Doppler dependent (as derived in Section II), it becomes desirable to have a Doppler-dependent solution. In this case, the azimuth subband decomposition strategy serves as a suitable approach. The requirement for a Doppler-dependent solution is also driven by the presence of the RCM effect, as in Section III-B.

The stacking strategy holds significant importance as it provides a larger number of samples to optimize the BSS performance, resulting in an unbiased estimation of the kurtosis. This requirement for a great number of samples is particularly relevant when the data tend to have a Gaussian distribution [49], and it is shown later in Section IV that the non-Gaussian characteristic of the range-compressed data is not adequately pronounced (as compared with the image data). Consequently, accumulating as many samples as feasible becomes preferable when dealing with the data that lack strong non-Gaussian traits. Stated differently, the stacking strategy serves as a suitable approach for acquiring supplementary samples from the limited azimuthal extension. The stacking strategy consists in reorganizing the SAR data, used as input for the BSS, and is proposed as follows:

$$D_{N_{\mathrm{az}} \times N_{\mathrm{rg}}} \rightarrow D_{N_{\mathrm{sta}} N_{\mathrm{az}} \times N_{\mathrm{rg}}/N_{\mathrm{sta}}} \tag{23}$$

where D denotes the data, N_{az} and N_{rg} are the total number of azimuth and range samples, and N_{sta} is the number of stacked azimuth lines, with $N_{\mathrm{rg}}/N_{\mathrm{sta}}$ being an integer number. The output data, obtained after the application of the BSS, are then organized in the original size. It is important to remark that reorganizing the data means grouping together N_{sta} azimuth lines, as illustrated in Fig. 7.

The optimum number of stacked azimuth lines must be evaluated empirically, as a tradeoff between the following contradicting requirements: on the one side, N_{sta} should be large to increase the robustness of the BSS method; on the other side, N_{sta} should be low in order to properly estimate the range dependent variations of the SAR mixing matrix.

The azimuth subband decomposition makes the proposed approach Doppler-dependent, and is introduced in order to account for: 1) the Doppler variations of

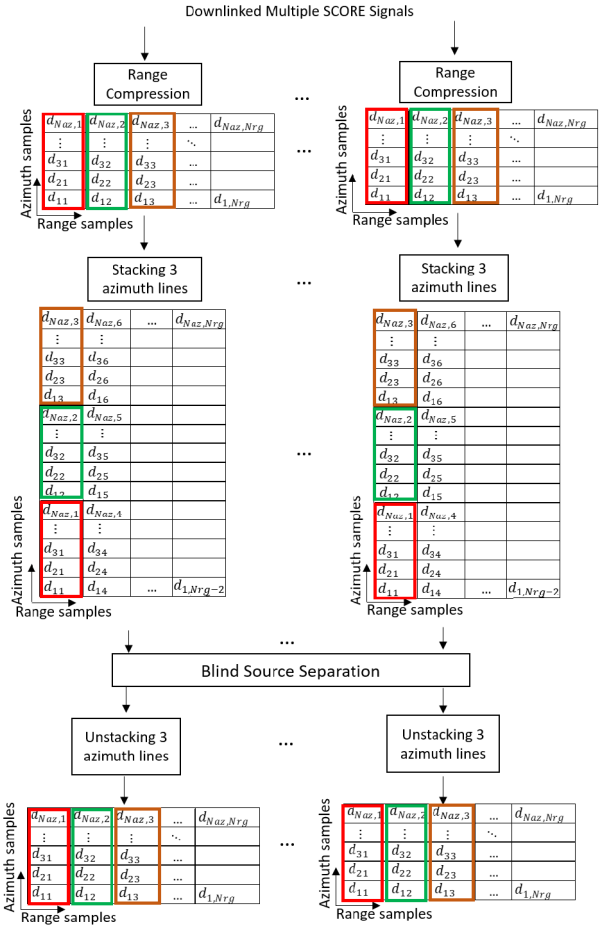

Fig. 7. Stacking strategy for $N_{\text{sta}} = 3$.

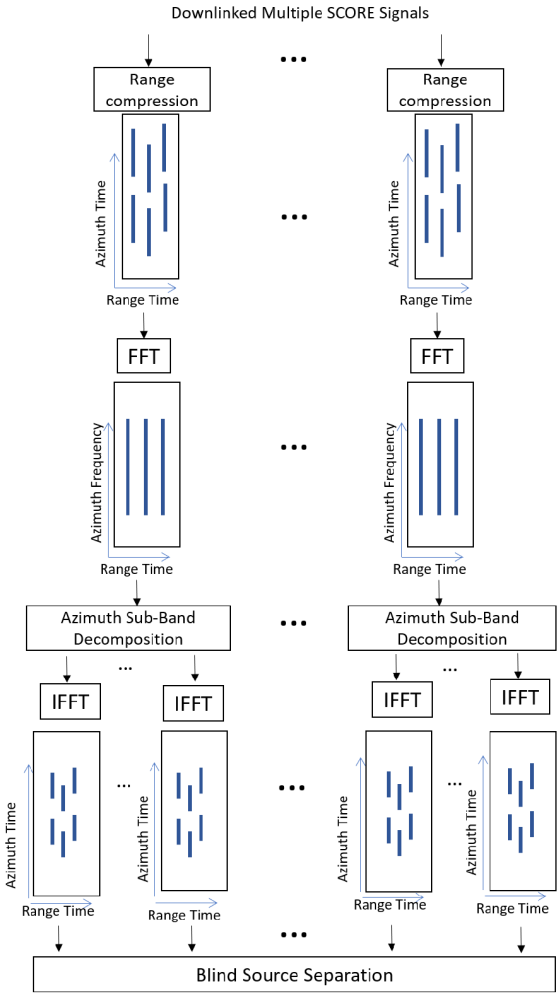

Fig. 8. Subband decomposition strategy.

the SAR mixing matrix and 2) the different, Doppler-dependent, reciprocity configurations, associated with the RCM (see Fig. 6).

It is worth to remark that the Gaussianity of the SAR data is typically higher in the Doppler domain than in the azimuth-time domain, due to the lower heterogeneity of the signal. Indeed, the Gaussianity of the SAR data depends also on the Doppler bandwidth: it increases for smaller Doppler bandwidths, i.e., coarser azimuth resolutions (see Table II for a numerical example). Accordingly, in order to optimize the BSS performance, the BSS is always applied in the (range- and azimuth-) time domain, rather than in the time-Doppler domain. In particular, the azimuth subband decomposition is implemented as follows (see Fig. 8): 1) the data are split into N_{sub} Doppler subbands in time-Doppler domain; 2) the data are transformed back into the time domain; 3) the BSS method is applied; and 4) the subbands are composed again to obtain the full Doppler bandwidth. The number of considered Doppler subbands, N_{sub}, must be optimized empirically, based on the following contradicting requirements: on the one side, N_{sub} shall be high in order to account for the mentioned Doppler-dependent variations; on the other side, N_{sub} must be low to limit the Gaussianity of the SAR data. The complete list of processing steps of the proposed method is illustrated in Fig. 9.

IV. Numerical Analysis

For the numerical analysis, let us refer to a DBF multichannel L-band SAR system, based on an array-fed reflector antenna, as the one described in Section II. The main system parameters are reported in Table I. The system is classified as high-resolution wide-swath (HRWS). It exploits five SCORE Rx beams, formed by activating sets of consecutive feed elements, to simultaneously image five subswaths. The overall swath extension on the ground is in the order of 300 km. A PRF of 2700 Hz and a processed Doppler bandwidth of 1348 Hz are used, in order to have a more noticeable effect of Doppler-dependent range ambiguity and RCM, leading to a 6-m azimuth resolution. Accordingly, five strong ambiguous echoes are received from the imaged swath. The reference system is designed in a manner similar to TDL [12], including a Tx/Rx module (TRM) with a peak power of 143 W and a reflector antenna with a 15-m diameter. The simulated data in this article are obtained using the SCORE technique, just like the implementation in TDL. Such a system design ensures a noise equivalent sigma zero (NESZ) below -25 dB.

The received radar data are simulated, according to the data model in (13), starting from the real-backscatter coefficients

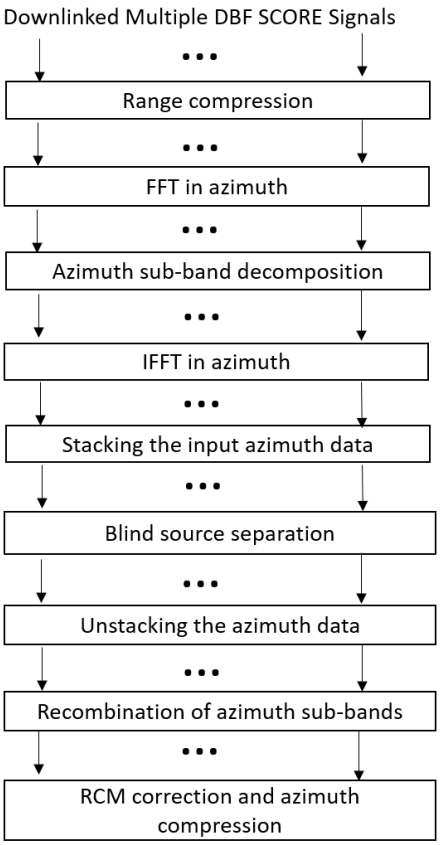

Fig. 9. Flowchart of the proposed method.

TABLE I
REFERENCE SYSTEM PARAMETERS

Parameter	Value
Orbit height	628 km
Platform velocity	7542 m/s
No. channels in elevation	35
Elevation tilt angle w.r.t. nadir	36 deg
Center frequency	1.26 GHz
PRF	2700 Hz
Chirp bandwidth	38 MHz
Processed Doppler bandwidth	1348 Hz
Pulse duration	30 μs
Number of sub-swaths	5
Signal-to-noise ratio	10 dB

provided by a calibrated SAR image.[4] In particular, as shown in Fig. 10, the raw data, range compressed data with uncorrected RCM, range compressed data with corrected RCM, and focused SAR image, are simulated. It is worth pointing out that the high-resolution wide-swath image would have a much higher number of samples than the SAR image used in this simulation. The width of each subswath is determined by $c \cdot \mathrm{PRI}/2 - c \cdot T_p$, where $c \cdot T_p$ refers to the blind range

[4]A single-SAR image of the TDX mission [50] has been used in this first demonstration of the new multibeam ambiguity suppression technique. A follow-on paper will provide a comprehensive in-depth investigation of the achievable ambiguity reduction performance for different terrain types using a large set of SAR data. The results from this comprehensive analysis are then used to develop a multichannel BSS calibration strategy to estimate the mixing coefficients in a robust manner over the whole swath and Doppler band.

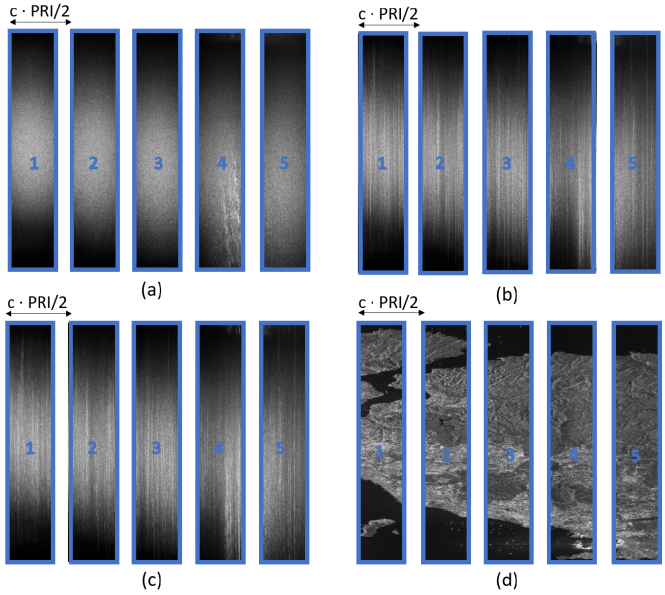

Fig. 10. Simulated SAR signals using a TanDEM-X (TDX) complex SAR image [50]. (a) Raw data. (b) Range compressed data with RCM correction. (c) Range compressed data with RCM. (d) Focused SAR image. The horizontal axis indicates the range direction, and the vertical the azimuth direction. For each case, five data segments are simulated, corresponding to areas separated by the distance of ambiguity. The performance of the proposed method will be analyzed later for the SAR data at different domains, i.e., raw data, range compressed with RCM and without RCM, and focused SAR image.

caused by the transmit event. The resulting width for each subswath is 46 km, which is equivalent to 5830 SAR image range samples after downsampling. To avoid border effects during the generation of raw data for the corresponding image, the width of each subswath is further extended by the pulse duration (corresponding to 1368 samples) on both the left and right sides, resulting in a total width of 8566 samples, including the extensions. However, due to the limited availability of SAR image data and to accelerate computation, only a segment of 7.1 km for each subswath is simulated. Specifically, the original SAR image is processed to obtain 4500 range samples (900 range samples for each of the five subswaths). The simulated segments are assumed to be spatially separated by the distance of the ambiguity. Finally, it is essential to note that each subswath is simulated and processed individually.

If not otherwise stated, and in order to obtain a realistic representation of the received signals, the mixing matrix in (13) is generated based on the antenna patterns of the TDL mission [2], [12]. To validate the method, the TDL pattern and its corresponding mixing matrix, as shown in Fig. 11, are considered as the actual pattern and actual mixing matrix, respectively. As can be seen, the mixing matrix is considerably low, with off-diagonal values between 0.0002 and 0.25, averaging at 0.05.

As regards the weak ambiguity signals s_{WA} in (13), the simulated range-ambiguous SAR data include one weak ambiguity from the far-range region and one weak ambiguity from the near-range region, which is realistic since the gain of the Tx pattern rapidly approaches zero as it moves outward from the illuminated swath. Specifically, only the ambiguity in the very

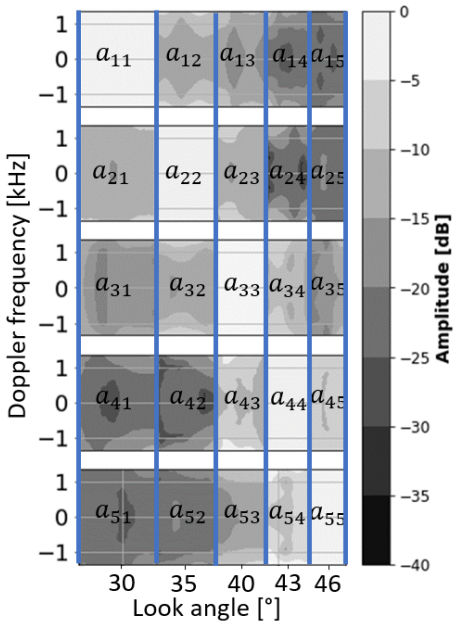

Fig. 11. Mixing matrix, $\mathbf{A}_{\mathrm{TDL}}$, extracted from TDL DBF antenna patterns. The blue vertical lines indicate the boundary between the simulated swath segments.

far range is expected to have a relatively high value. This reflects the imperfect attenuation of range ambiguities in the far range by the Tx pattern.[5] In fact, here the angular separation between useful signal and ambiguity reduces. As regards the additive white Gaussian noise in (13), a realistic scenario characterized by an SNR of 10 dB is considered.

The performance of the proposed method is evaluated with reference to the SAR image quality, as the RASR of the focused SAR image

$$\mathrm{RASR}(k) = \frac{\sum_{j=0}^{N_a-1} \left| x''(k,j) - s''(k,j) \right|^2}{\sum_{j=0}^{N_a-1} |s''(k,j)|^2} \tag{24}$$

where k denotes the range sample index; j is the azimuth sample index; N_a is the number of azimuth samples; $x''(k,j)$ is the complex value of the received image; and $s''(k,j)$ is the complex value of the useful image. When evaluating the RASR after applying the method, the received image x'' is replaced by the ambiguity-suppressed image $\hat{s}''$.

Before starting with the analysis of the performance of the proposed method for range ambiguity suppression, a few considerations about the Gaussianity of the simulated useful source signals are presented. The Gaussianity is evaluated for the simulated L-band source signals by using the complex signal kurtosis (CSK) metric [51]: a zero CSK corresponds to a complex Gaussian distribution; a negative to a sub-Gaussian; a positive to a super-Gaussian [52]. Accordingly, when the CSK values depart from 0, the signal is expected to become less Gaussian, which is favorable for the method.

The obtained results are reported in Table II. It can be seen that the RCM correction makes the data, both raw and range-compressed, more Gaussian as compared with when RCM is not corrected. Furthermore, raw data are more Gaussian than the range-compressed data, while the focused SAR image is significantly more non-Gaussian. Additionally, the range-compressed data in the Doppler domain is considerably more Gaussian as compared with the range-compressed data in the azimuth-time domain. The Doppler bandwidth reduction also causes the data more Gaussian, as shown by the lower CSK value of the range-compressed data with reduced Doppler bandwidth.

[5]The issue could be solved by either having a better shape of the Tx pattern or adding an additional auxiliary Rx beam to collect appropriate data from the far-range distance.

TABLE II
CSK FOR DIFFERENT KINDS OF SAR DATA

Type of SAR Data	Domain	CSK
Raw data without RCM Correction	Range-time, Doppler	0.43
Range compressed without RCM Correction	Range-time, Doppler	0.83
Raw data with RCM Correction	Time	1.0
Raw data without RCM Correction	Time	1.6
Range compressed with RCM correction	Time	1.71
Range compressed without RCM Correction	Time	1.96
Fully focused data	Time	8.41
Range compressed with 30% Doppler bandwidth, without RCM Correction	Time	1.15

In order to investigate the dependence of the BSS performance on the SAR data, it is useful to first refer to a very simple mixing matrix, with no dependence on the range time and Doppler frequency (25), as shown at the bottom of the next page.

This is similar to the mixing matrix in the classical cocktail party problem.

Fig. 12 shows for this simple and artificial case the performance of the selected JADE BSS method, when applied to the simulated received raw data (with and without RCM correction), range compressed data (with and without RCM correction), range compressed data in the range-Doppler domain, and the focused SAR image. Specifically, it reports the RASR in (24) for the simulated SAR image after the application of the JADE BSS and, as a comparison, the RASR of the simulated received SAR image. First of all, from Fig. 12(a)–(d), it can be seen that the BSS method achieves better performance when applied to (raw and range-compressed) data without RCM correction, rather than to data with RCM correction. Moreover, the BSS completely fails, when applied to the focused SAR image, as shown in 12(f). This can be justified by the reciprocity property, which is violated after RCM correction and/or azimuth focusing (see Section III). In order to further clarify the joint impact of reciprocity and Gaussianity on the BSS performance, it is useful to relate Fig. 12 with Table II. From Fig. 12(b) and (c), it can be seen that the reciprocity may have a more pronounced effect than Gaussianity: even if the raw data without RCM correction in Fig. 12(b), compared with the range-compressed data with RCM correction in Fig. 12(c), exhibits higher Gaussianity, as indicated by the lower CSK value in Table II (1.6 versus 1.71), they allow to achieve a better RASR suppression. However, when no RCM is applied, the BSS achieves better performance on the range-compressed data, rather than on the raw data, as shown by Fig. 12(b) and (d). This can be

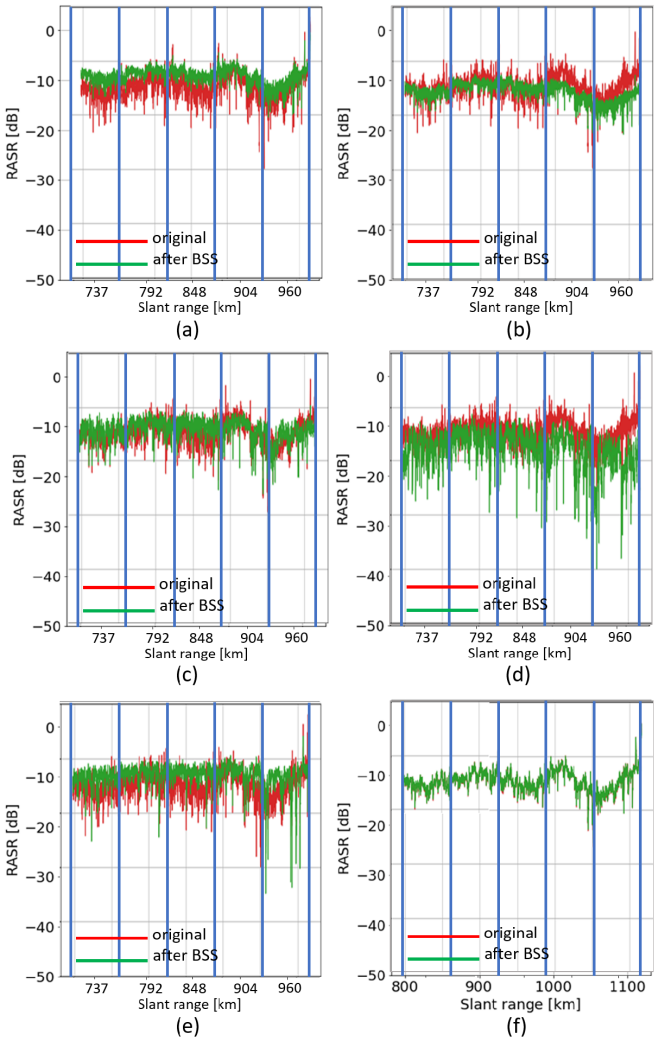

Fig. 12. RASR performance for input SAR data simulated using A_{SIM}. The JADE BSS is applied to different SAR data domains. (a) Raw data with RCM correction (CSK = 1.0). (b) Raw data without RCM correction (CSK = 1.6). (c) Range compressed data with RCM correction (CSK = 1.71). (d) Range compressed data without RCM correction (CSK = 1.96). (e) Range compressed in the range-Doppler domain without RCM correction (CSK = 0.83). (f) Focused SAR image (CSK = 8.41). The blue vertical lines indicate the boundary between the simulated swath segments. The red curve shows the RASR for the original simulated SAR image; the green curve shows the RASR for the ambiguity-suppressed image (after applying JADE BSS method). In (f), the red curve is covered by the green curve.

attributed to the lower Gaussianity of the range-compressed data, compared with the raw data (CSK of 1.96 versus 1.6). Fig. 12(e) shows a degradation in performance in the range-Doppler domain. This is due to the high Gaussianity level (CSK = 0.83) in the Doppler domain compared with the time domain (see Table II). Overall, Fig. 12 indicates that the best

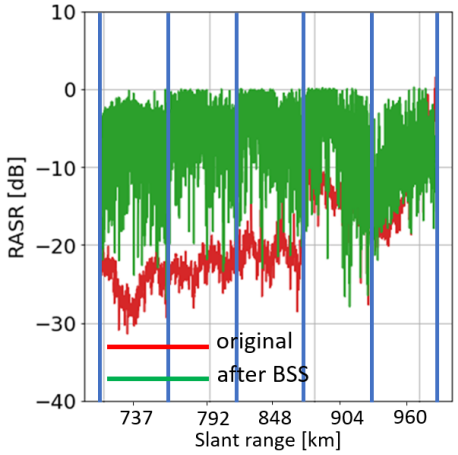

Fig. 13. RASR performance for input SAR data simulated using A_{TDL}. The JADE BSS is applied to range-compressed data with RCM. The blue vertical lines indicate the boundary between the simulated swath segments. The red curve shows the RASR for the original simulated SAR image; the green curve the RASR for the ambiguity-suppressed image (after applying JADE BSS method).

RASR suppression is achieved from the range-compressed data with uncorrected RCM. From now on the performance analysis refers to the range-compressed data with RCM.

Let us now evaluate the JADE BSS performance in the reference scenario, i.e., by considering the realistic mixing matrix $\mathbf{A}_{\mathrm{TDL}}$ obtained from the TDL antenna patterns [6]. The obtained results are reported in Fig. 13. It is worth to remark that the off-diagonal elements have two relevant characteristics (see Fig. 11): 1) their value strongly varies, especially along the range direction and 2) they can reach very low values of -35 dB. This makes the successful application of the BSS method very challenging, as can be seen in Fig. 13. The comparison between Figs. 12(c) and 13 further evidences the dramatic effect of the mixing matrix on the BSS performance. These first results highlight that a reliable evaluation of the BSS performance must be based on a realistic mixing matrix. In particular, the strong 2-D dependence of the SAR mixing matrix on range and azimuth cannot be neglected (see Section II).

As shown in Fig. 13, a mere application of the BSS does not allow suppression of the range ambiguities when a realistic SAR mixing matrix is considered. Let us then additionally apply the proposed stacking optimization strategy. The obtained results are plotted in Fig. 14, for different values of the number of stacked azimuth lines: $N_{\mathrm{sta}} = 0, 30, 100, 900$. The improvement introduced by the stacking strategy is evident.

The dependence of the RASR performance on the number of stacked azimuth lines is further investigated in Fig. 15,

$$\mathbf{A}_{\mathrm{SIM}} = \begin{bmatrix} 1 & 0.3+0.3j & 0.23+0.11j & 0.17+0.15j & 0.2+0.1j \\ 0.2+0.2j & 1 & 0.32+0.21j & 0.23+0.1j & 0.18+0.15j \\ 0.23+0.21j & 0.3+0.2j & 1 & 0.2+0.1j & 0.15+0.09j \\ 0.17+0.15j & 0.23+0.11j & 0.3+0.2j & 1 & 0.1+0.3j \\ 0.2+0.1j & 0.17+0.15j & 0.23+0.11j & 0.3+0.2j & 1 \end{bmatrix}. \quad (25)$$

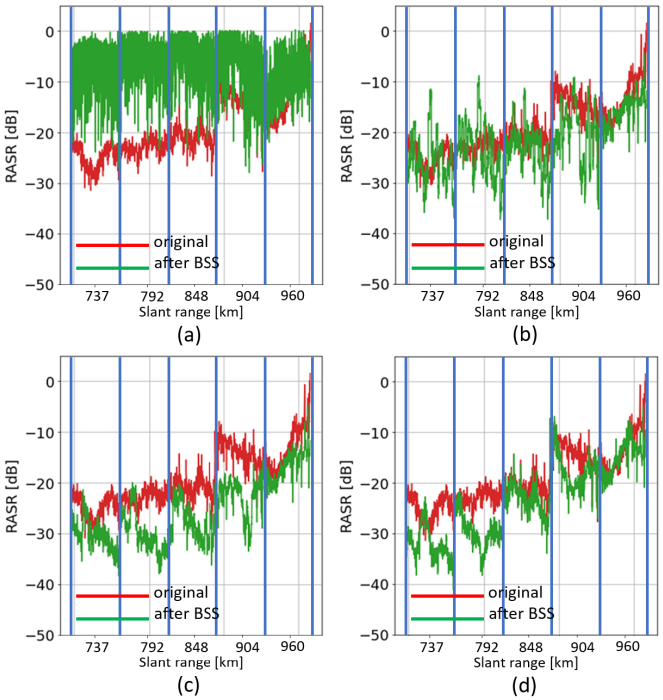

Fig. 14. Assessment of stacking optimization strategy by RASR performance. The BSS is applied to the range-compressed data with RCM. The number of stacked azimuth lines is: (a) $N_{\text{sta}} = 0$; (b) $N_{\text{sta}} = 30$; (c) $N_{\text{sta}} = 100$; and (d) $N_{\text{sta}} = 900$.

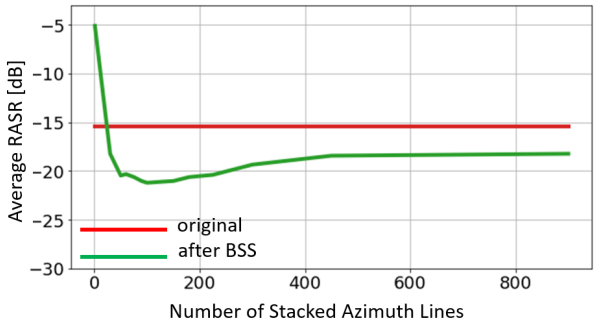

Fig. 15. Average RASR performance versus number of stacked azimuth lines. The BSS is applied to range compressed data with RCM.

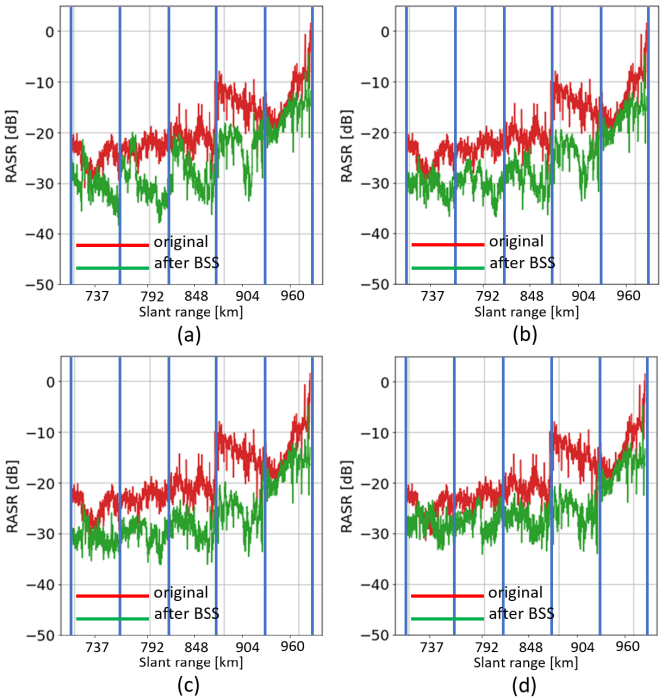

Fig. 16. Assessment of azimuth-sub bands decomposition strategy by RASR performance. The BSS is applied to the range-compressed data with RCM. The stacking strategy ($N_{\text{sta}} = 100$) and the number of azimuth subbands is: (a) $N_{\text{sub}} = 1$; (b) $N_{\text{sub}} = 3$; (c) $N_{\text{sub}} = 7$; and (d) $N_{\text{sub}} = 15$.

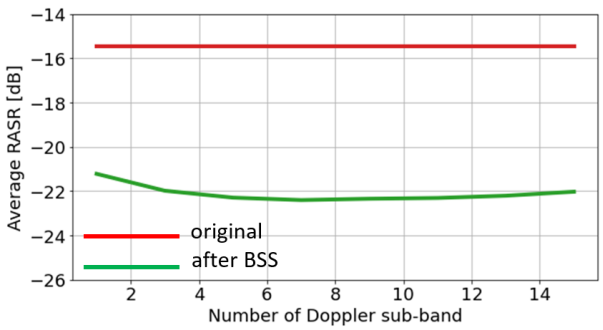

Fig. 17. Average RASR performance versus number of azimuth subbands. The BSS is applied to range compressed data with RCM.

by means of the average RASR

$$\overline{\text{RASR}} = \frac{1}{N_r} \sum_{k=0}^{N_r-1} \text{RASR}(k) \tag{26}$$

where k denotes range sample index and N_r is the number of range samples. Fig. 15 indicates the necessity of empirical analysis when dealing with the stacking strategy due to contradicting requirements (see Section III-C). Three conclusions can be drawn: 1) until $N_{\text{sta}} = 100$, the stacking strategy results in significant improvement in RASR performance, despite the range-dependent variations of the SAR mixing matrix; 2) from $N_{\text{sta}} = 100$, the degradation due to range dependent variations surpasses the improvement; and 3) from $N_{\text{sta}} = 450$, the degradation is comparable to the improvement. Fig. 15 shows that the optimum number of stacked azimuth lines for this system is 100. However, it is important to note that one could avoid the stacking approach to obtain a sufficient number of data samples and use instead more data in azimuth from longer data takes when available.

Let us now include also the azimuth subband decomposition. The obtained results are shown in Fig. 16, for different values of the number of subbands: $N_{\text{sub}} = 1, 3, 7, 15$. The best result is achieved for $N_{\text{sub}} = 7$, as can be seen by comparing Fig. 16(a) and (c). In particular, around the slant range of 790 and 840 km, the improvement for $N_{\text{sub}} = 7$ is about 8 dB compared with the case of $N_{\text{sub}} = 1$.

Fig. 16 highlights also that the RASR is worse in the far-range subswath compared with the RASR in the other subswaths. This is due to the contribution of the weak ambiguity in far range, which is still significant enough for this subswath.

The obtained results show that the azimuth subbands produce a lower improvement in the performance, compared with the stacking strategy. This is justified by the fact that the antenna pattern values, weighting the ambiguous signals,

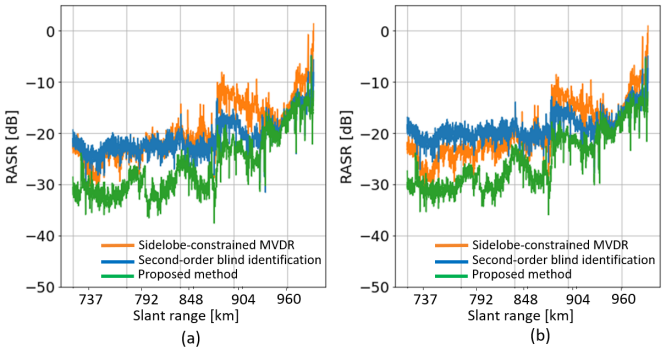

Fig. 18. Comparison of the proposed method with others, considering data with: (a) SNR = 15 dB and (b) SNR = 10 dB. The orange curve represents the sidelobe-constrained MVDR [53], the blue curve indicates SOBI BSS in [23], and the green curve represents the proposed method. The spatial separation between the simulated swath segments is not visualized.

already help suppress the range ambiguity components in the nonzero-Doppler region.

The dependence of the RASR performance on the number of azimuth subbands is further investigated in Fig. 17, by means of the average RASR. The impact of the number of azimuth subbands on the RASR performance can be associated with four aspects: the variation of A_{TDL} along the Doppler direction, the RCM, the gain of the antenna pattern in nonzero Doppler, and the statistics of the subband data. Based on this analysis, two conclusions can be drawn: 1) until $N_{\mathrm{sub}} = 7$, the improvement due to the variation of A_{TDL} and RCM effect, as discussed in Section III, outweighs the degradation due to the increased Gaussianity within the subband data and 2) beyond $N_{\mathrm{sub}} = 7$, the degradation is greater than the improvement. Accordingly, the optimum number of azimuth subbands for this system is 7. In particular, for $N_{\mathrm{sub}} = 7$ and $N_{\mathrm{sta}} = 100$, the proposed method achieves an improvement of range ambiguity suppression of 6 dB on average.

Upon comparing Figs. 15 and 17, it becomes evident that the RASR performance improvement achieved through the stacking strategy is considerably greater than that obtained from the azimuth subband decomposition strategy. This is due to the effectiveness of the stacking strategy in providing a large number of data, which is a significant factor responsible for improving the performance of the BSS technique. Additionally, it is worth mentioning that the optimum number of stacked azimuth lines and azimuth subbands depends mainly on the assumed antenna patterns. Specifically, on how the main-to-sidelobe ratio changes versus range and azimuth. Accordingly, the obtained values should be valid also for similar antenna architectures.

V. Discussion

To highlight the advantage of the proposed method over other range ambiguity suppression techniques, various comparisons are presented. Foremost, it is essential to inform that the accurate information about the antenna pattern is crucial for the successful implementation of most other range ambiguity suppression methods. One of the sources of inaccuracies in the antenna pattern knowledge arises from digital channel errors. An investigation conducted in [53] reveals that when using the sidelobe-constraint MVDR technique to suppress

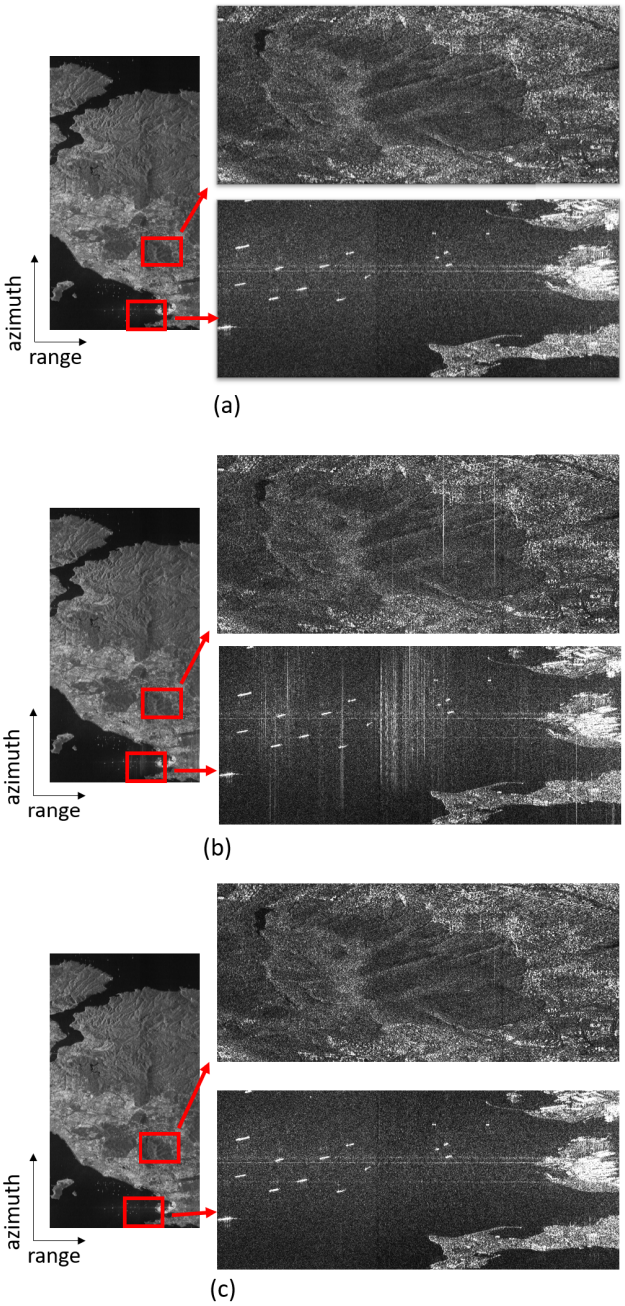

Fig. 19. Simulated SAR images. (a) Ambiguity-free image. (b) Ambiguous image. (c) Ambiguity-suppressed image. The horizontal axis indicates the range direction, the vertical axis azimuth. The spatial separation between the simulated swath segments is not visualized.

range ambiguities, where digital channel errors are present, the range ambiguity suppression performance can degrade by up to 10 dB for array-fed reflector antennas and up to 30 dB for planar antennas.

Another range ambiguity suppression technique, LCMV null-steering, is also addressed in [15], considering the impact of topographic errors. These topographic errors can cause a mismatch in the null steering, which is typically positioned in the direction of range ambiguity. In the example provided in [15], a terrain height offset of 1.5 km results in a significant increase in ambiguities, up to −17 dB.

The examples of the MVDR and LCMV techniques previously mentioned only focus on specific errors, namely, digital channel error and topographic error, respectively. However, it is important to recognize that there are many other errors that collectively contribute to the inaccuracy of the actual antenna pattern in real-world scenarios. Some of these errors include thermoelastic deformation [54], pattern uncertainty, pulse extension loss, pulse extension over range, and pulse bandwidth [55]. When all these errors are considered, one could reasonably expect that the actual antenna pattern deviates significantly from the ideal pattern, potentially leading to a significant degradation of range ambiguity suppression performance.

APC is another type of technique [7] that can be influenced by the knowledge of the antenna pattern. Additionally, the technique is affected by the oversampling factor [8]. In contrast, the proposed method exhibits performance independence with respect to the oversampling factor. This means that the method's effectiveness remains consistent, regardless of the specific oversampling factor, making it less susceptible to variations in the multichannel configuration. Another phase encoding technique, known as waveform-encoded SAR [56], is specifically suitable for scenarios with a very high range ambiguity-to-signal ratio, which are not common in real-world scenarios.

The multifrequency subpulse (MFSP) method [57] exploits the radar signal bandwidth to increase the imaged swath extension, without the emergence of range ambiguities. This technique does not rely on knowledge of the antenna pattern. Nevertheless, it is designed for burst modes (ScanSAR/TOPS) and may not be well-suited for imaging a very wide swath with high resolution in the stripmap mode, due to limitations imposed by the power constraints and by the available signal bandwidth.

Furthermore, it is also worth recalling that the significance of this article is also referred to its adoption of a realistic data model for formulating the range ambiguity problem. Specifically, the model employs a complex-valued mixing matrix with dependencies in both range-time and Doppler-frequency directions, in contrast to the approach in [22] and [23], which utilizes a real-valued mixing matrix and incorporates only stationary values. Moreover, as explained in Section III, the proposed higher order BSS is expected to provide a better robustness to noise, compared with a second-order BSS approach, as the one in [22] and [23].

In order to further, numerically, clarify the advantages of the proposed method, it is useful to refer to Fig. 18. Here, two methods for range ambiguity suppression are considered as relevant benchmarks: the sidelobe-constrained MVDR in [53], which requires the knowledge of the antenna pattern; the BSS approach-based second-order blind identification (SOBI) in [23], that does not need any knowledge of the antenna pattern. To ensure more realistic input data, that account for inaccuracies in knowledge of the antenna pattern, digital channel errors are included, with phase error standard deviation levels $\sigma_\zeta = 40^\circ$ and magnitude standard deviation levels $\sigma_\xi = 0.2$, as described in [53]. Furthermore, two scenarios with different noise levels are simulated: one with a mean SNR of 15 dB and one with 10 dB. It is important to note that both SNR values are realistic for advanced HRWS L-band systems with an NESZ of -25 dB, considering that SAR data can have varying SNR values depending on incident angle and polarization type [58], [59]. The obtained results are reported in Fig. 18(a) and (b), respectively, for the case of SNR $= 15$ and 10 dB. They show that that the proposed method outperforms the other ones in both the simulated scenarios. In particular, an improvement up to 10 dB in the near range can be achieved. Moreover, as expected from [36], [37], and [38], the proposed method demonstrates a higher robustness against noise than the BSS based on SOBI in [23]: even in the case where the data is noisier, i.e., SNR $= 10$ dB, the proposed method continues to perform well, whereas the method in [23] show a degradation up to about 3 dB.

Finally, a qualitative assessment of the achieved ambiguity suppression is provided in Fig. 19. It shows a comparison between the simulated ambiguity-free SAR image, the ambiguous SAR image with an average RASR of 15 dB, and the ambiguity-suppressed SAR image (the spatial separation between the simulated swath segments is here not visualized, for simplicity). To highlight the achieved ambiguity suppression, a closer view of the areas marked by red boxes is taken. These show the noticeable improvement achieved by the proposed method, especially over backscattering surfaces, characterized by a low intensity, such as the sea, affected by a strong ambiguous disturbance.

VI. Conclusion

This article tackles the problem of range ambiguity suppression in advanced high-resolution wide-swath SAR systems employing multiple elevation beams.

The range ambiguity suppression is mathematically described as a 2-D problem and it has been shown that there exists a close connection to the cocktail party phenomenon. In particular, for the first time, the range-time and Doppler-frequency dependence of the received signals is included in the multichannel data model by using an equivalent 2-D antenna radiation pattern that accounts for both the pattern variations in azimuth and the time-dependent beamforming in elevation. To suppress the range ambiguities, a novel solution, based on the higher order BSS, is presented. The method is applied on ground, without impacting the SAR instrument complexity. The performance of the proposed method is numerically analyzed, with reference to an array-fed reflector antenna SAR system, by simulating a realistic acquisition scenario. To this aim, real-SAR data and the actual antenna patterns of the TDL mission proposal are considered. The obtained results show that the proposed method can improve the average range ambiguity-to-signal ratio by about 6 dB. An even larger improvement is expected for low intensity backscattering surfaces, like that of the sea, typically characterized by a high-range ambiguity disturbance. These promising results demonstrate that the proposed method provides a new and effective tool for range ambiguity suppression in SAR systems operating with multiple elevation beams. A systematic and in-depth performance comparison for a variety of different SAR scenes will be the subject of a follow-on paper together

with the development of an associated calibration strategy for multichannel SAR systems.

REFERENCES

[1] J. C. Curlander and R. N. McDonough, *Synthetic Aperture Radar*, vol. 11. New York, NY, USA: Wiley, 1991.

[2] A. Moreira et al., "Tandem-L: A highly innovative bistatic SAR mission for global observation of dynamic processes on the earth's surface," *IEEE Geosci. Remote Sens. Mag.*, vol. 3, no. 2, pp. 8–23, Jun. 2015.

[3] K. Kellogg et al., "NASA-ISRO synthetic aperture radar (NISAR) mission," in *Proc. IEEE Aerosp. Conf.*, Mar. 2020, pp. 1–21.

[4] M. Younis and W. Wiesbeck, "SAR with digital beamforming on receive only," in *Proc. IEEE Int. Geosci. Remote Sens. Symp.*, Jun. 1999, pp. 1773–1775.

[5] M. Suess, B. Grafmueller, and R. Zahn, "A novel high resolution, wide swath SAR system," in *Proc. IEEE Int. Geosci. Remote Sens. Symp. (IGARSS)*, Jul. 2001, pp. 1013–1015.

[6] S. Huber, M. Younis, A. Patyuchenko, G. Krieger, and A. Moreira, "Spaceborne reflector SAR systems with digital beamforming," *IEEE Trans. Aerosp. Electron. Syst.*, vol. 48, no. 4, pp. 3473–3493, Oct. 2012.

[7] J. Dall and A. Kusk, "Azimuth phase coding for range ambiguity suppression in SAR," in *Proc. IEEE Int. Geosci. Remote Sens. Symp.*, vol. 3, Sep. 2004, pp. 1734–1737.

[8] F. Bordoni, M. Younis, and G. Krieger, "Ambiguity suppression by azimuth phase coding in multichannel SAR systems," *IEEE Trans. Geosci. Remote Sens.*, vol. 50, no. 2, pp. 617–629, Feb. 2012.

[9] M. Villano, G. Krieger, and A. Moreira, "Waveform-encoded SAR: A novel concept for nadir echo and range ambiguity suppression," in *Proc. 12th Eur. Conf. Synth. Aperture Radar*, Jun. 2018, pp. 1–6.

[10] M. Villano, G. Krieger, and A. Moreira, "Staggered SAR: High-resolution wide-swath imaging by continuous PRI variation," *IEEE Trans. Geosci. Remote Sens.*, vol. 52, no. 7, pp. 4462–4479, Jul. 2014.

[11] M. Villano, G. Krieger, and A. Moreira, "Ambiguities and image quality in staggered SAR," in *Proc. IEEE 5th Asia–Pacific Conf. Synth. Aperture Radar (APSAR)*, Sep. 2015, pp. 204–209.

[12] S. Huber, F. Q. de Almeida, M. Villano, M. Younis, G. Krieger, and A. Moreira, "Tandem-L: A technical perspective on future spaceborne SAR sensors for Earth observation," *IEEE Trans. Geosci. Remote Sens.*, vol. 56, no. 8, pp. 4792–4807, Aug. 2018.

[13] F. Feng, S. Li, W. Yu, P. Huang, and W. Xu, "Echo separation in multidimensional waveform encoding SAR remote sensing using an advanced null-steering beamformer," *IEEE Trans. Geosci. Remote Sens.*, vol. 50, no. 10, pp. 4157–4172, Oct. 2012.

[14] Q. Zhao et al., "Echo separation for space-time waveform-encoding SAR with digital scalloped beamforming and adaptive multiple null-steering," *IEEE Geosci. Remote Sens. Lett.*, vol. 18, no. 1, pp. 92–96, Jan. 2021.

[15] G. Krieger et al., "CEBRAS: Cross elevation beam range ambiguity suppression for high-resolution wide-swath and MIMO-SAR imaging," in *Proc. IEEE Int. Geosci. Remote Sens. Symp. (IGARSS)*, Jul. 2015, pp. 196–199.

[16] G. Krieger et al., "In-orbit relative amplitude and phase antenna pattern calibration for Tandem-L," in *Proc. 12th Eur. Conf. Synth. Aperture Radar*, 2018, pp. 1–6.

[17] J. Reimann, M. Schwerdt, K. Schmidt, N. T. Ramon, and B. Döring, "The DLR spaceborne SAR calibration center," *Frequenz*, vol. 71, nos. 11–12, pp. 619–627, Jan. 2017.

[18] M. Schwerdt, B. Brautigam, M. Bachmann, B. Doring, D. Schrank, and J. Hueso Gonzalez, "Final TerraSAR-X calibration results based on novel efficient methods," *IEEE Trans. Geosci. Remote Sens.*, vol. 48, no. 2, pp. 677–689, Feb. 2010.

[19] S. Haykin and Z. Chen, "The cocktail party problem," *Neural Comput.*, vol. 17, no. 9, pp. 1875–1902, Sep. 2005.

[20] E. J. Amin, M. Younis, and G. Krieger, "Blind source separation: A novel range ambiguity suppression method in multichannel SAR," in *Proc. ARSI Adv. Remote Sens. Instrum. Conf.*, 2019.

[21] E. Amin, M. Younis, and G. Krieger, "Two-dimensional range ambiguity suppression in multichannel SAR using blind source separation method," in *Proc. 13th Eur. Conf. Synth. Aperture Radar*, Mar. 2021, pp. 1–5.

[22] S. Chang, Y. Deng, Y. Zhang, Q. Zhao, R. Wang, and K. Zhang, "An advanced scheme for range ambiguity suppression of spaceborne SAR based on blind source separation," *IEEE Trans. Geosci. Remote Sens.*, vol. 60, 2022, Art. no. 5230112.

[23] S. Chang et al., "An advanced echo separation scheme for space-time waveform-encoding SAR based on digital beamforming and blind source separation," *Remote Sens.*, vol. 14, no. 15, p. 3585, Jul. 2022.

[24] C. Jutten and J. Herault, "Blind separation of sources, Part I: An adaptive algorithm based on neuromimetic architecture," *Signal Process.*, vol. 24, no. 1, pp. 1–10, Jul. 1991.

[25] A. Freeman et al., "SweepSAR: Beam-forming on receive using a reflector-phased array feed combination for spaceborne SAR," in *Proc. IEEE Radar Conf.*, May 2009, pp. 1–9.

[26] M. Villano, G. Krieger, and A. Moreira, "Nadir echo removal in synthetic aperture radar via waveform diversity and dual-focus postprocessing," *IEEE Geosci. Remote Sens. Lett.*, vol. 15, no. 5, pp. 719–723, May 2018.

[27] O. Dogan et al., "Double dual focusing for range ambiguity suppression-experimental results," in *Proc. 14th Eur. Conf. Synth. Aperture Radar*, Jul. 2022, pp. 1–6.

[28] F. Bordoni, G. Krieger, and D. Lind, "Radiometric degradation associated with terrain height variations and pulse duration in scan-on-receive SAR images," *IEEE Trans. Geosci. Remote Sens.*, vol. 60, 2022, Art. no. 5223214.

[29] G. Krieger, N. Gebert, and A. Moreira, "Multidimensional waveform encoding: A new digital beamforming technique for synthetic aperture radar remote sensing," *IEEE Trans. Geosci. Remote Sens.*, vol. 46, no. 1, pp. 31–46, Jan. 2008.

[30] G. Krieger, "MIMO-SAR: Opportunities and pitfalls," *IEEE Trans. Geosci. Remote Sens.*, vol. 52, no. 5, pp. 2628–2645, May 2014.

[31] A. Hyvärinen and E. Oja, "Independent component analysis: Algorithms and applications," *Neural Netw.*, vol. 13, nos. 4–5, pp. 411–430, Jun. 2000.

[32] L. Tong, V. C. Soon, Y. F. Huang, and R. Liu, "AMUSE: A new blind identification algorithm," in *Proc. IEEE Int. Symp. Circuits Syst.*, May 1990, pp. 1784–1787.

[33] A. Belouchrani, K. Abed-Meraim, J.-F. Cardoso, and E. Moulines, "A blind source separation technique using second-order statistics," *IEEE Trans. Signal Process.*, vol. 45, no. 2, pp. 434–444, Feb. 1997.

[34] P. Comon, "Independent component analysis, a new concept?" *Signal Process.*, vol. 36, no. 3, pp. 287–314, Apr. 1994.

[35] J. F. Cardoso and A. Souloumiac, "Blind beamforming for non-Gaussian signals," *IEE Proc. F Radar Signal Process.*, vol. 140, no. 6, pp. 362–370, 1993.

[36] M. H. Fatnan, Z. M. Hussain, and H. R. Mohammed, "Blind source separation under semi-white Gaussian noise and uniform noise: Performance analysis of ICA, Sobi and JadeR," *A A*, vol. 21, no. 2, p. 22, 2019.

[37] N. Liu, J. Li, Q. Liu, H. Su, and W. Wu, "Blind source separation using higher order statistics in kernel space," *COMPEL, Int. J. Comput. Math. Electr. Electron. Eng.*, vol. 35, no. 1, pp. 289–304, Jan. 2016.

[38] S. Liu, B. Wang, and L. Zhang, "Blind source separation method based on neural network with bias term and maximum likelihood estimation criterion," *Sensors*, vol. 21, no. 3, p. 973, Feb. 2021.

[39] G. H. Golub and C. F. Van Loan, *Matrix Computations*, vol. 3. Baltimore, MD, USA: The Johns Hopkins Univ. Press, 2013.

[40] A. Papoulis, *Probability and Statistics*. Upper Saddle River, NJ, USA: Prentice-Hall, 1990.

[41] J. Shlens, "A tutorial on independent component analysis," 2014, *arXiv:1404.2986*.

[42] S. Choi and A. Cichocki, "Blind separation of nonstationary and temporally correlated sources from noisy mixtures," in *Proc. IEEE Signal Process. Society Workshop*, Dec. 2000, pp. 405–414.

[43] V. Vigneron, A. Paraschiv-Ionescu, A. Azancot, O. Sibony, and C. Jutten, "Fetal electrocardiogram extraction based on non-stationary ICA and wavelet denoising," in *Proc. 7th Int. Symp. Signal Process. Appl.*, 2003, pp. 69–72.

[44] E. Forootan, J. Kusche, M. Talpe, C. K. Shum, and M. Schmidt, "Developing a complex independent component analysis (CICA) technique to extract non-stationary patterns from geophysical time series," *Surv. Geophys.*, vol. 39, no. 3, pp. 435–465, May 2018.

[45] J. Fischer, U. Benz, and A. Moreira, "Efficient SAR raw data compression in frequency domain," in *Proc. IEEE Int. Geosci. Remote Sens. Symp.*, vol. 4, Jun. 1999, pp. 2261–2263.

[46] A. C. Frery, H.-J. Muller, C. C. F. Yanasse, and S. J. S. Sant'Anna, "A model for extremely heterogeneous clutter," *IEEE Trans. Geosci. Remote Sens.*, vol. 35, no. 3, pp. 648–659, May 1997.

[47] G. Gao, "Statistical modeling of SAR images: A survey," *Sensors*, vol. 10, no. 1, pp. 775–795, Jan. 2010.

[48] I. G. Cumming and F. H. Wong, "Digital processing of synthetic aperture radar data," *Artech House*, vol. 1, no. 3, pp. 108–110, 2005.

[49] J. M. Herrmann and F. J. Theis, "Statistical analysis of sample-size effects in ICA," in *Proc. Int. Conf. Intell. Data Eng. Automated Learn.* Cham, Switzerland: Springer, 2007, pp. 416–425.
[50] G. Krieger et al., "TanDEM-X: A satellite formation for high-resolution SAR interferometry," *IEEE Trans. Geosci. Remote Sens.*, vol. 45, no. 11, pp. 3317–3341, Nov. 2007.
[51] X. Leng, K. Ji, S. Zhou, and X. Xing, "Ship detection based on complex signal kurtosis in single-channel SAR imagery," *IEEE Trans. Geosci. Remote Sens.*, vol. 57, no. 9, pp. 6447–6461, Sep. 2019.
[52] E. Ollila, J. Eriksson, and V. Koivunen, "Complex elliptically symmetric random variables—Generation, characterization, and circularity tests," *IEEE Trans. Signal Process.*, vol. 59, no. 1, pp. 58–69, Jan. 2011.
[53] S. Huber, M. Younis, G. Krieger, and A. Moreira, "Error analysis for digital beamforming synthetic aperture radars: A comparison of phased array and array-fed reflector systems," *IEEE Trans. Geosci. Remote Sens.*, vol. 59, no. 8, pp. 6314–6322, Aug. 2021.
[54] K. Mouthaan, "Digital beamforming for spaceborne reflector SAR systems via FIR filter networks in the presence of uncertainties," Ph.D. dissertation, TU Berlin, Berlin, Germany, 2017.
[55] F. Q. de Almeida, "Multichannel staggered SAR for high-resolution wide-swath imaging," Ph.D. dissertation, Deutsches Zentrum Für Luft-Und Raumfahrt, Oberpfaffenhofen, Germany, 2018.
[56] L. Dell'Amore, M. Villano, and G. Krieger, "Assessment of image quality of waveform-encoded synthetic aperture radar using real satellite data," in *Proc. 20th Int. Radar Symp. (IRS)*, Jun. 2019, pp. 1–10.
[57] F. Bordoni, G. Krieger, and M. Younis, "Multifrequency subpulse SAR: Exploiting chirp bandwidth for an increased coverage," *IEEE Geosci. Remote Sens. Lett.*, vol. 16, no. 1, pp. 40–44, Jan. 2019.
[58] D. D'Aria, D. Giudici, A. M. Guarnieri, P. Rizzoli, and J. Medina, "A wide swath, full polarimetric, L band spaceborne SAR," in *Proc. IEEE Radar Conf.*, May 2008, pp. 1–4.
[59] H. Skriver, "Land-cover map information from polarimetric SAR using knowledge-based techniques," in *Proc. 3rd Int. Symp. Retr. Bio Geophys. Parameters SAR Data Land Appl.*, vol. 475, U. K. Sheffield, A. Wilson, and S. Quegan, Eds. Noordwijk, The Netherlands: ESA, 2002, pp. 105–110.

Ershad Junus Amin received the B.Eng. degree in electrical and electronic engineering from Nanyang Technological University, Singapore, in 2011, and the M.T. degree in electrical engineering from the Bandung Institute of Technology (ITB), Bandung, Indonesia, in 2014. Since 2018, he has been with the Microwaves and Radar Institute at the German Aerospace Centre, Weßling, Germany.

From 2013 to 2017, he was a Radar Engineer with PT Sembada Karya Mandiri, Bandung, a private defense company, where he was involved in the development of radar processing modules within the combat management system. He was a Freelancer as a Radar System Engineer, where he was involved in developing digital signal processing and plan position indicator modules. His research interests include spaceborne multichannel synthetic aperture radar (SAR) systems, SAR processing for high-resolution wide-swath SAR systems, digital beamforming, echo separation techniques, and range ambiguity suppression.

Gerhard Krieger (Fellow, IEEE) received the Dipl.-Ing. (M.S.) degree and Dr.-Ing. (Ph.D.) degree (Hons.) in electrical and communication engineering from the Technical University of Munich, Munich, Germany, in 1992 and 1999, respectively.

From 1992 to 1999, he was with the Ludwig Maximilians University, Munich, where he conducted multidisciplinary research on neuronal modeling and nonlinear information processing in biological and technical vision systems. Since 1999, he has been with the Microwaves and Radar Institute of the German Aerospace Center, Oberpfaffenhofen, Germany, where he started as a Research Associate developing signal processing algorithms for a novel forward-looking radar system employing digital beamforming on receive. From 2001 to 2007, he led the New SAR Missions Group, which pioneered the development of advanced bistatic and multistatic radar systems, such as TanDEM-X, and innovative multichannel SAR techniques and algorithms for high-resolution wide-swath SAR imaging. Since 2008, he has been the Head of the Radar Concepts Department, which currently hosts about 50 scientists focusing on new SAR techniques, missions, and applications. He has been serving as a Mission Engineer for TanDEM-X. He made also major contributions to the development of the Tandem-L mission concept, where he led the Phase-0 and Phase-A studies. Since 2019, he has been a Professor with Friedrich-Alexander-University-Erlangen-Nuremberg, Erlangen, Germany. He has authored or coauthored more than 100 peer-reviewed journal articles, nine invited book chapters, about 500 conference papers, and more than 20 patents.

Prof. Krieger received several national and international awards, including two best paper awards from the European Conference on Synthetic Aperture Radar, two TRANSACTIONS Prize Paper Awards from the IEEE Geoscience and Remote Sensing Society, and the W. R. G. Baker Prize Paper Award from the IEEE Board of Directors. In 2014, he served as the Technical Program Chair for the European Conference on Synthetic Aperture Radar and a Guest Editor for the IEEE JOURNAL OF SELECTED TOPICS IN APPLIED EARTH OBSERVATIONS AND REMOTE SENSING. He has been an Associate Editor of the IEEE TRANSACTIONS ON GEOSCIENCE AND REMOTE SENSING since 2012.

Marwan Younis (Fellow, IEEE) received the B.Sc. degree in electrical engineering from the University of Baghdad, Baghdad, Iraq, in 1992, and the Dipl.-Ing. (M.Sc.) and Dr.-Ing. (Ph.D.) degrees in electrical engineering from the Karlsruhe Institute of Technology (KIT), Karlsruhe, Germany, in 1997 and 2004, respectively.

In 1996, he was an Intern with the Jet Propulsion Laboratory, Pasadena, CA, USA, where he spent research sabbaticals in 2013 and 2019, respectively. From 1998 to 2004, he was a Research Scientist with the Institut für Höchstfrequenztechnik und Elektronik, KIT. Since 2005, he has been with the Microwaves and Radar Institute of the German Aerospace Center, Oberpfaffenhofen, Germany. He is currently the Head of the SAR Techniques Group, German Aerospace Center (DLR), Oberpfaffenhofen, Germany, and a Professor of spaceborne radar systems with KIT. He is currently a DLR Senior Scientist. He has authored and coauthored about 200 conference papers, 46 reviewed publications, and holds five patents. His research interests include synthetic aperture radar (SAR) systems and techniques, MIMO SAR, digital beamforming, SAR performance, calibration, and antennas.

Dr. Younis is an Active Member of the IEEE and the Geoscience and Remote Sensing Society (GRSS). He served the GRSS AdCom from 2018 until 2020. He received the Hermann Billing Award for his Ph.D. thesis in 2005. He was the Chair of the Instrumentation and Future Technologies GRSS Technical Committee. He is a reviewer of the IEEE publications. He was an Associate Editor of the IEEE GEOSCIENCE AND REMOTE SENSING LETTER form 2012 to 2019.

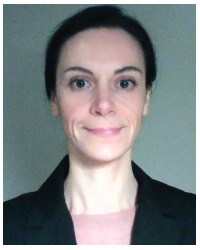

Federica Bordoni received the Laurea (M.S.) degree in telecommunication engineering and the Ph.D. degree in information engineering from the University of Pisa, Pisa, Italy, in 2001 and 2005, respectively.

From 2002 to 2004, she was with the Department of Ingegneria dell'Informazione, University of Pisa, where her research activity included modern spectral estimation and detection techniques for multichannel and multidata signal processing, with applications both in the field of synthetic aperture radar (SAR) interferometry and radar surveillance. From 2004 to 2004, she was a Visiting Research Scholar with Karlstad University, Karlstad, Sweden. From 2005 to 2007, she was with Thales Alenia Space Italia, Rome, Italy, with the validation/certification of COSMO-SkyMed SAR products. Since 2007, she has been with the Microwaves and Radar Institute, German Aerospace Center (DLR), Oberpfaffenhofen, Germany. She has authored or coauthored more than 50 refereed journals and conference papers. Her research interests include innovative multichannel spaceborne SAR systems with digital beamforming capability, novel advanced operational modes for high-resolution wide-swath SAR imaging, and SAR imaging performance analysis.

André Barros Cardoso da Silva was born in Taubaté, Brazil, in 1986. He received the B.S. (summa cum laude) degree in telecommunication engineering from the University of Taubaté, Taubaté, in 2009, the M.S. degree in electronic engineering from the Instituto Tecnológico de Aeronáutica, São José dos Campos, Brazil, in 2013, and the Dr.-Ing. (Ph.D.) degree (magna cum laude) in electrical engineering from the Karlsruhe Institute of Technology, Karlsruhe, Germany, in 2019.

From 2005 to 2009, he joined the Brazilian National Institute for Space Research, São José dos Campos, as an Engineering Intern, where he was involved in data collection platforms for the Brazilian Environmental Data Collection System satellites. From 2010 to 2014, he was a Research Engineer with the Brazilian Antarctic Program (PROANTAR) on five missions during the summer seasons (228 days in total), where he was involved in the activation and maintenance of atmospheric radars and data collection systems for environmental monitoring in the Brazilian Antarctic Station Comandante Ferraz, Antarctica. Since 2014, he has been with Microwaves and Radar Institute, German Aerospace Center, Weßling, Germany, first as a Ph.D. Fellow and then a Research Scientist. His research interests include high-resolution airborne/spaceborne SAR processing, end-to-end SAR simulation, moving target indication over land and ocean, along-track interferometry, and space-time adaptive processing methodologies.

Dr. Barros Cardoso da Silva received the honorable mention in telecommunication and the CREA-SP Professional Formation Award from the Brazilian Regional Council of Engineering and Architecture of São Paulo state for first-class students in engineering courses in 2010.

Alberto Moreira (Fellow, IEEE) received the bachelor's and master's degrees in electrical engineering from the Aeronautical Technological Institute, São José dos Campos, Brazil, in 1984 and 1986, respectively, and the Ph.D. degree (Hons.) from the Technical University of Munich, Munich, Germany, in 1993.

From 1996 to 2001, he was the Head of the Synthetic Aperture Radar (SAR) Technology Department, German Aerospace Center (DLR), Oberpfaffenhofen, Germany. Under his leadership, the DLR airborne SAR system has been upgraded to operate in innovative imaging modes, such as polarimetric SAR interferometry, tomography, and holography. Since 2001, he has been the Director of the Microwaves and Radar Institute, DLR, and a Professor with the Karlsruhe Institute of Technology, Karlsruhe, Germany, in the field of microwave remote sensing. His DLR's Institute contributes to several scientific programs and projects for spaceborne SAR missions, including TerraSAR-X, TanDEM-X, SAR-Lupe, and SARah, Kompsat-6, PAZ, Sentinel-1, BIOMASS, ROSE-L, Harmony, Sentinel-1NG, Envision, and VERITAS. The mission TanDEM-X, led by his Institute, has generated a global, high-resolution digital elevation model of the Earth with unprecedented accuracy, for which he is the initiator and Principal Investigator (PI) for this mission. He has served as a member for the ESA Mission Advisory Groups of ENVISAT/ASAR, Sentinel-1, and Hydroterra. He is currently serving as a member of the Science Study Team for the ESA's EnVision mission. He has authored or coauthored more than 500 publications in international conferences and journals, eight book chapters, and holds more than 45 international patent grants in the radar and antenna fields. His research interests include spaceborne radar end-to-end system design, microwave techniques and system concepts, signal processing, and remote sensing applications.

Prof. Moreira served as the President for the IEEE Geoscience and Remote Sensing Society (GRSS) in 2010. He and his colleagues received the GRSS TRANSACTIONS Prize Paper Awards in 1997, 2001, and 2007, and the GRSS LETTERS Prize Paper Award in 2015 and 2017, respectively. He was also a recipient of several international awards, including the IEEE Aerospace and Electronic Systems Society Fred Nathanson Award in 1999, the IEEE Kiyo Tomiyasu Technical Field Award in 2007, the IEEE W. R. G. Baker Award from the IEEE Board of Directors in 2012, the IEEE GRSS Distinguished Achievement Award in 2014, and the IEEE Dennis J. Picard Medal for Radar Technologies and Applications in 2023. He served as the General Chair for European Conference on Synthetic Aperture Radar in 2006 and the General Co-Chair for IGARSS in 2012. He was the Founder and the Chair of the GRSS German Chapter from 2003 to 2008. He has been serving as the Chair for the Major Awards of GRSS since 2017. He served as an Associate Editor for the IEEE GEOSCIENCE AND REMOTE SENSING LETTERS from 2003 to 2007. He has been serving as an Associate Editor for the IEEE TRANSACTIONS ON GEOSCIENCE AND REMOTE SENSING (since 2005).